Journal of Alloys and Compounds

Catalytic action and bactericidal behavior of samarium/carbon spheres-doped manganese oxide nanostructures and their molecular docking analysis

--Manuscript Draft--

Manuscript Number:	JALCOM-D-23-05877R2
Article Type:	Full Length Article
Keywords:	Catalyst, bactericidal, samarium/carbon, molecular docking
Corresponding Author:	Walid Nabgan Rovira i Virgili University Tarragona, Tarragona SPAIN
First Author:	Ehtasham Ul Haq
Order of Authors:	Ehtasham Ul Haq
	Muhammad Imran
	Ali Haider
	Anum Shahzadi
	Ayesha Habib
	Anwar Ul-Hamid
	Walid Nabgan
	Majed A. Bajaber
	Muhammad Ikram
Abstract:	The co-precipitation technique was adapted to synthesize different concentrations (2 and 4 %) of samarium (Sm) doped constant equates of carbon spheres (Cs) and manganese oxide (MnO2). The principal objective of this investigation is to demonstrate confirmation that Sm/Cs-doped MnO2 nanostructures (NSs) owned antibacterial and catalytic attributes. Reduction in surface area manifested to agglomeration, NSs faces become inaccessible to initiate a reaction, can be overcome upon doping of Sm. Sm has the potential to increase the activity of metal oxide ascribed to its electron trapping effect. The structural morphologies, optical properties, functional groups, elemental composition, and d-spacing were determined by applying various characterizations. With the incorporation of CS and Sm, UV-vis spectra shifted towards lower wavelength and band gap energy (Eg) was reduced. MnO2 possessed orthorhombic structure, according to the XRD pattern and TEM exhibited long Burr-like morphology of undoped MnO2. SAED image illustrated that MnO2 is polycrystalline. 4% Sm/CS doped MnO2 revealed the highest degradation (91%) in a neutral environment. Furthermore, 4% Sm/Cs doped-MnO2 revealed an inhibitory zone of 2.85 mm against Escherichia coli (E. coli). Additionally, an analysis of molecular docking revealed a binding interface with NRs and the functional domains of certain cellular proteins. Results indicated that Cs-doped MnO2 and Cs/Sm-doped MnO2 NRs are the most potent DNA gyrase and FabB enzyme inhibitors.
Order of Authors:	Ehtasham Ul Haq
	Muhammad Imran
	Ali Haider
	Anum Shahzadi
	Ayesha Habib
	Anwar Ul-Hamid
	Walid Nabgan
	Majed A. Bajaber

	Muhammad Ikram

Modification in MnO_2 optical and catalytic properties with rare earth metal and Carbonaceous spheres has been excepted as an promising methodology for better waste water remediation against RhB, , to the best of our comprehension , no publication has been reported on this.

In this study, reference samples and Sm/Cs doped-MnO_2 NSs have been prepared by co-precipitation approach. Antimicrobial action against E. coli and dye removal from water were studied using synthesized samples. The detailed analysis of the ternary system was observed by a variety of characterizations

Reviewer #3: The revised version is much better now. However, the author did not take my comment No. 5 seriously and did not calculate the % crystallinity and % porosity for all the prepared materials. Moreover, it is better to provide the Scherrer relation and determine the specific surface area of all materials through their diffraction data. More than merely stating the grain size or particular surface area derived from calculations is required. It is essential to provide a comprehensive scientific explanation for the observed greater surface area and lower grain size. This explanation in the discussion part should be supported with the most relevant and up-to-date references, [5] Materials, 135 (2023) 113192; RSC Advances, 13 (2023) 28063-28075; Ceramics International, 49 (2023) 32377-32387; Ceramics International, 49 (2023) 27827-27836 and Zeitschrift für Physikalische Chemie, 237 (2023) 1325-1344.

Ans: As per suggestion, recommented points have been mentioned in the manuscript on pages 9 and 10.

Dopant-free and Sm/Cs doped-MnO_2 NSs were synthesized.

Sm/Cs-doped MnO_2 nanostructures (NSs) owned antibacterial and catalytic attributes.

Cs/Sm doped MnO_2 was proposed as a potential blocker of FabB and DNA gyrase enzymes.

Credit Author Statement

Ehtasham Ul Haq- methodology, writing the original draft

Muhammad Imran- Supervision, resources

Ali Haider- investigation, methodology, resources

Anum Shahzadi- Software, conceptualization, review and editing

Ayesha Habib- data curation, methodology, resources

Anwar Ul-Hamid- methodology, visualization

Walid Nabgan- conceptualization, visualization

Majed A. Bajaber- investigation, review and editing

Muhammad Ikram- data curation, review and editing, resources, fund acquisition

Declaration of interests

☒ The authors declare that they have no known competing financial interests or personal relationships that could have appeared to influence the work reported in this paper.

☐The authors declare the following financial interests/personal relationships which may be considered as potential competing interests:

Catalytic action and bactericidal behavior of samarium/carbon spheres-doped manganese oxide nanostructures and their molecular docking analysis

Ehtasham Ul Haq[a], Muhammad Imran[a], Ali Haider[b], Anum Shahzadi[c], Ayesha Habib[d], Anwar Ul-Hamid[e], Walid Nabgan[f*], Majed A. Bajaber[g], Muhammad Ikram[d*]

[a]Department of Chemistry, Government College University, Faisalabad, Sahiwal Road, Sahiwal, Punjab, 57000, Pakistan
[b]Department of Clinical Sciences, Faculty of Veterinary and Animal Sciences, Muhammad Nawaz Shareef, University of Agriculture, Multan 66000, Punjab, Pakistan
[c]Department of Pharmacy, COMSATS University Islamabad, Lahore Campus, Lahore 54000, Pakistan
[d]Solar Cell Applications Research Lab, Department of Physics, Government College University Lahore, Lahore 54000, Punjab, Pakistan
[e]Core Research Facilities, King Fahd University of Petroleum & Minerals, Dhahran 31261, Saudi Arabia
[f]Departament d'Enginyeria Química, Universitat Rovira i Virgili, Av Països Catalans 26, 43007 Tarragona, Spain
[g]Chemistry Department, Faculty of Science, King Khalid University, P.O. Box 9004, Abha 61413, Saudi Arabia

Corresponding authors email: [d]dr.muhammadikram@gcu.edu.pk, [f]wnabgan@gmail.com

Abstract

The co-precipitation technique was adapted to synthesize different concentrations (2 and 4 %) of samarium (Sm) doped constant equates of carbon spheres (Cs) and manganese oxide (MnO_2). The principal objective of this investigation is to demonstrate confirmation that Sm/Cs-doped MnO_2 nanostructures (NSs) owned antibacterial and catalytic attributes. Reduction in surface area manifested to agglomeration, NSs faces become inaccessible to initiate a reaction, can be overcome upon doping of Sm. Sm has the potential to increase the activity of metal oxide ascribed to its electron trapping effect. The structural morphologies, optical properties, functional groups, elemental composition, and d-spacing were determined by applying various characterizations. With the incorporation of CS and Sm, UV-vis spectra shifted towards lower wavelength and band gap energy (Eg) was reduced. MnO_2 possessed orthorhombic structure, according to the XRD pattern and TEM exhibited long Burr-like morphology of undoped MnO_2. SAED image illustrated that MnO_2 is polycrystalline. 4% Sm/CS doped MnO_2 revealed the highest degradation (91%) in a neutral environment. Furthermore, 4% Sm/Cs doped-MnO_2 revealed an inhibitory zone of 2.85 mm against *Escherichia coli* (*E. coli*). Additionally, an analysis of molecular docking revealed a binding interface with NRs and the functional domains of certain cellular proteins. Results indicated that Cs-doped MnO_2 and Cs/Sm-doped MnO_2 NRs are the most potent DNA gyrase and FabB enzyme inhibitors.

Keywords: Catalyst, bactericidal, samarium/carbon, molecular docking

INTRODUCTION

In the time of scientific innovation and industrial development, the environment is mainly the victim of industrial by-products. Water pollution is a major environmental problem that gets worse over time. Organic wastes, likely dyes, are the utmost dischargeable impurities in water, which threaten lives. It may cause severe damage to the kidney, liver, and central nervous system (CNS). Dyes, including Rhodamine B (RhB), methyl orange (MO), methylene blue, and congo red, are toxic, with mutagenic and carcinogenic effects on humans and ecosystems [1]. Mastitis incurs significant financial implications for the dairy industry. It's attributed to abnormalities in milk's microbiome, chemistry, physical alterations, and structural modifications to the mammary glandular pad. Pathogens, including *E. coli* and *Staphylococcus aureus* (*S. aureus*), can evolve from various sources like the host, atmosphere, season, and typical pathogen [2,3]. The parasitic microbes reproduce rapidly, eradicating indigenous aquatic species and harming the ecosystem by lowering dissolved oxygen levels [4,5]. Several techniques, such as adsorption, catalysis, advanced oxidation process [6], ozonation [7], irradiation, and photocatalysis [8,9], can be used for wastewater treatment. Several theories have been proposed on the mechanisms behind the influence of metallic nanoparticles (MNPs) on microbial enzymes. These theories include the disruption of microbial enzymes caused by metal ion liberation, changes in membrane integrity resulting in penetration into the bacterial cytoplasm, accumulation within the periplasmic space, and direct influence by reactive oxygen species (ROS) produced as a result of MNP exposure [10]. Catalysis is a cost-effective, environment-friendly, and energy-efficient process [11].

In the last few years, semiconductor nanomaterials (NMs) have aroused considerable interest in environmental development for researchers. Two-dimensional (2D) materials, including MoS_2, BN, GO, MnO_2, and WS_2, are currently being employed to improve water purification [12–14]. MnO_2 is naturally abundant, low toxic, and cheaper [15]. MnO_2 is one of the most attractive inorganic materials owing to its structural and physical characteristics, broad implementations in energy storage, catalysis [15], antimicrobial activity, ion exchange, biosensors, and molecular sieves [16]. However, MnO_2 has a wider bandgap, which limits its ability to absorb visible light. Consequently, several strives have been to improve MnO_2's antibacterial capacity and dye degradation effectiveness[17]. Dang's group synthesized MnO_2-coated diatomite composite via a wet-chemical technique to evaluate the degradation rate of MO and MB [18]. Fathy et al. employed a co-precipitation methodology to prepare MnO_2/MWCNT nanocomposite catalyst and assessed the oxidative decolorization of RB19 dye [19]. To improve the dye degradation, other publications on metal oxides doped with RE metal ions are also published as Eu-doped ZnO [20], Gd-doped TiO_2 [21], Gd-doped ZnO [22], and Sm-doped ZnO [23]. This study focuses on Sm doping in MnO_2 for better Catalytic activity. Sm ions (Sm^{2+} and Sm^{3+}) can potentially upgrade metal oxide activities ascribed to trapping electrons [24]. Carbon spheres are a significant candidate for a novel form of catalytic support because of their abundance of surface functional groups, including carboxylic, hydroxyl, and carbonyl groups. For example, carbon spheres have been employed as a support for the immobilizing of metal oxides, metal sulphides and metals [25]. Modification in MnO_2 optical and catalytic properties with rare earth metal and Carbonaceous spheres has been excepted as an promising methodology for better waste water remediation against RhB, , to the best of our comprehension , no publication has been reported on this.

In this study, reference samples and Sm/Cs doped-MnO_2 NSs have been prepared by co-precipitation approach. Antimicrobial action against *E. coli* and dye removal from water were studied using synthesized samples. The detailed analysis of the ternary system was observed by a variety of characterizations

2 EXPERIMENTAL SECTIONS

2.1 Materials

Manganese (II) sulfate monohydrate ($MnSO_4.H_2O$, 99%, Panreac*)*, Potassium per-manganate ($KMnO_4$, 99.5%, AnalaR), Sodium hydroxide (NaOH, 98%) had received from Sigma-Aldrich. Samarium (III) nitrate hexa-hydrate (Sm $(NO_3)_3.6H_2O$, 99.9%, Alfa-Aesar) were used as purchased.

2.2 Synthesis of Cs

The hydrothermal carbonization method was utilized to prepare Cs. A 1 M glucose solution was prepared at continual stirring to attain the desired transparent and straightforward solution. The aqueous solution was autoclaved at 180 ˚C for 12 h. Cs were recovered by washing the accompanied precipitates with DI water and drying them overnight at 100 ˚C, as shown in Fig. 1a.

2.3 Synthesis of MnO_2 and Sm/Cs doped-MnO_2

Co-precipitation was employed to synthesize MnO_2 NSs using 0.5 M of $MnSO_4.H_2O$ and $KMnO_4$, stirred vigorously at 80 ˚C. The pH remained steady at 12 with a dropwise inclusion of

1 M NaOH. The precipitates were washed out by centrifugation twice (7 min at 7000 rpm) under continuous stirring, heated overnight at 150 ˚C, and crushed to obtain MnO_2 fine powder. Similarly, the procedure mentioned above was followed to synthesize distinct concentrations (2 and 4%) of Sm-doped fixed amounts of Cs into MnO_2, as portrayed in Fig. 1b.

2.4 Catalysis

The CA of pristine and Sm/Cs doped-MnO_2 was performed using 400 L of Sodium borohydride ($NaBH_4$) as the reductant and 3 mL of newly prepared MB solution as the oxidant. Consequently, 400 mL of synthesized samples were added to the above solution. Decolorization of RhB into LRhB was observed at predictable spans. The degradation rate was studied by UV-vis spectrophotometer, and the %age of dye degradation was assessed as follows [26]:

$$\% \text{ Degradation} = \frac{C_0 - C_t}{C_o} \times 100 \text{ ------------------- } (1)$$

2.5 Segregation and Identification of MDR *E. coli*

2.5.1 Specimens Assortment

Raw milk samples from selected dairy cattle were collected by direct milking into disinfected glassware marketed at various veterinary hospitals, markets, and farms in Punjab, Pakistan. Plain milk was transferred to the laboratory promptly after being retrieved at 4 ˚C. The coliforms in raw milk were enumerated on MacConkey agar. Plates were incubated for 48 h at 37 ˚C.

2.5.2 Recognition and Differentiation of Bacteria

Gram staining and various biochemical procedures were executed to validate the initial recognition of *E. coli* based on the colony shape seen, as described in Bergey's Manual of Determinative Bacteriology [27].

2.5.3 Antibiotic susceptibility

Disk diffusion was used by Bauer et al. [28] over Mueller Hinton agar to test antibiotic susceptibility (MHA). Antibiotic resistance of *E. coli* was determined by performing a test on the subsequent antibiotics (classes); Tetracycline (Te) 30 µg (Tetracyclines), Amoxycillin (A) 30 µg (Penicillins), Ciprofloxacin (Cip) 5 µg (Quinolones), Gentamicin (Gm) 10 µg (Aminoglycosides), Azithromycin (Azm) 15 µg (Macrolides), Ceftriaxone (Cro) 30 µg (Cephalosporins) and Imipenem (Imi) 10 µg (Carbapenem), [29]. The turbidity of *E. coli* decontaminated colonies was set to 0.5 MacFarland. In addition, the contaminated plates were spread-plated over Muller Hinton Agar (MHA) to avoid the antibiotic plates from overlaying their inhibitory domains. After 24 hours of incubation at 37°C, the findings were interpreted in accordance with the criteria established by the Clinical and Laboratory Standard Institute [30]. Bacteria that showed resistance to at least three different antibiotics were classified as multidrug-resistant [31].

2.5.4 Antibacterial Evaluation

Using agar well diffusion technology, in vitro bactericidal action of pristine and Sm/Cs doped-MnO_2 was assessed by MDR *E. coli* reflective strains collected from mastitis milk. The 0.5 McFarland norm of MDR *E. coli* was swabbed onto Macconkey agar dishes. A septic cork borer was adopted to construct 6 mm diameter holes in agar. Developed materials were employed at both mild (0.5 mg/50 µl) and higher (1.0 mg/50 µl) concentrations. We accordingly employed dilutions of ciprofloxacin (0.005 mg/50 µl) and DI water (50 µl) as positive and negative standards [32].

2.5.5 Statistical analysis

Inhibition region widths (in mm) were used to determine antibacterial efficacy, and single-way variance analysis (ANOVA) employing SPSS 20 was implemented for the statistical evaluation [33].

2.7 Molecular Docking Analysis

Molecular binding investigation of Cs-doped MnO_2 and Cs/Sm-doped MnO_2 was studied. This was done by focusing on integral proteins for microbial progression and maintenance. Binding analysis was subjected to several protein targets from different biosynthetic processes, including DNA gyrase$_{E. coli}$ and -ketoacyl- [acyl carrier protein] synthase I. (FabB) B$_{E. coli}$. DNA gyrase is critical in producing genetic material and folic acid, essential for microbial resilience. FabB catalyzes critical stages in bacterial cells' fatty acid biosynthesis pathway [34–36]. Crystal structures of *E. coli* target proteins were obtained using a protein data library (Fig. S5). Protein Data Bank was examined for structures of DNA gyrase B$_{E. coli}$ (PDB ID: 4PRV), resolution:1.45 [37], and -ketoacyl- [acyl carrier protein] synthase I (FabB) B$_{E. coli}$ (PDB ID: 1FJ4),) resolution:2.35 [38]. The binding analysis was performed with SYBYL-X 2.0 software suite [39]. SYBYL-X 2.0 was utilized to create 3D frameworks of compounds and assess the binding capacities of nanorods with the active domain motifs of chosen proteins, the same as it had been employed in our prior studies [40,41].

3 RESULTS AND DISCUSSION

Cs were synthesized using hydrothermal carbonization, illustrated in Fig. 1a. Various Sm concentrations (2 and 4 wt.%) were doped into Cs/MnO_2 via the co-precipitation route, as shown in Fig. 1b.

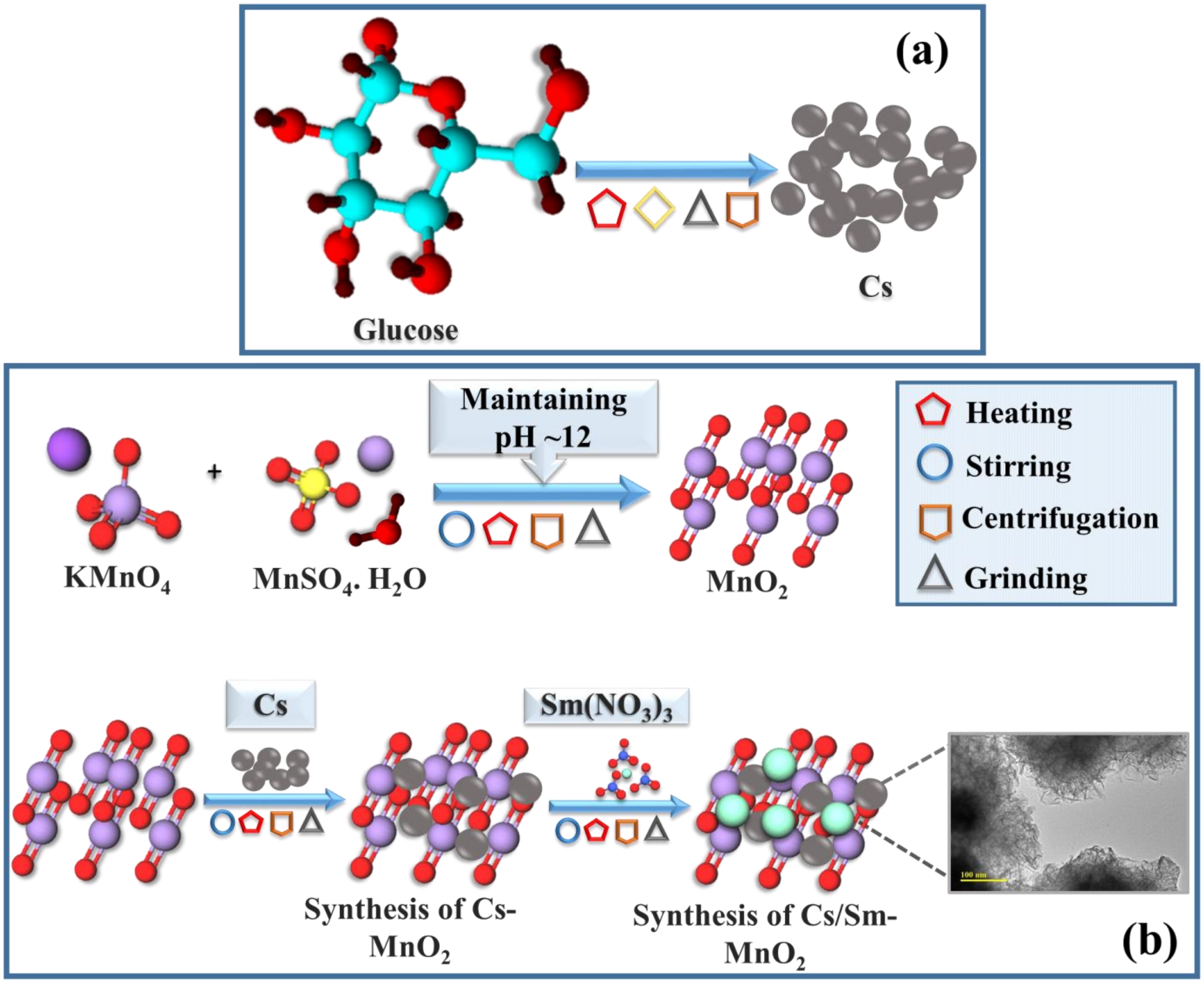

Fig. 1: (a) Schematic synthesis of Cs and (b) integration of Sm/Cs-doped MnO_2.

Fig. 2a illustrates the structural properties and phase purity of MnO_2 and Sm/Cs-doped MnO_2 NSs employing XRD patterns. Bragg Peaks sited at 21.70° (110), 36.95° (021), 44.42° (220), 49.32° (230), 55.36° (221), 66.05° (241), and 79.09° (022) confirmed the orthorhombic structure of MnO_2 by (JCPDF 01-073-1539/00-039-0375). Moreover, peaks at 28.05° (212) and 32.27° (103) attributed to Mn_2O_3 and Mn_2O_4, respectively advocated by (01-073-1826/00-024-0734). Upon doping of Cs, peaks broadening were noticed, attributed to their small crystal size. Peak broadening is also associated with amorphous carbon and low-degree graphitization [42]. The intensity of peaks decreased and broadened upon the incorporation of 2% Sm into MnO_2 as it inhibits the growth of the MnO_2 lattice, in line with earlier reports [43]. However, the higher doping of Sm increased the peak intensity, which implies that Sm integration may be advantageous to the growth of preferential orientation [44]. Using the Debye-Scherer formula calculated the grain (crystallite) size of prepared samples as mentioned below [45]:

$$\text{G.S} = \frac{k\lambda}{\beta Cos\theta}$$

The grain size of MnO_2, Cs doped-MnO_2, and (2 and 4 wt.%)Sm/Cs doped-MnO_2 was measured as 14.60, 12.67, 9.89, and 12.92 nm respectively.

The specimens' surface area was computed using the following equation [46]:

$$\text{Surface area} = \frac{6000}{G.S \times \rho x}$$

The surface area of MnO_2, Cs doped-MnO_2, and (2 and 4 wt. %)Sm/Cs doped-MnO_2 is 96, 97, 156.43, and 119.38 m^2/g.

As crystallite size increases, surface characteristics such as specific surface area and surface-to-volume ratio decrease [47]. In smaller grains, deformation occurs due to changes in the surface state of the boundary [48] which is why surface area increases and vice versa.

The following relationship was used to compute the percentage crystallinity of as-synthesized specimens [49]:

$$\text{\% Crystallinity} = \frac{Area\ under\ the\ crystalline\ peak}{Area\ of\ all\ peaks}$$

The pristine MnO_2, Cs doped-MnO_2, and (2 and 4%)Sm/Cs doped-MnO_2 had a calculated crystallinity of 55.63, 30.34, 29.89, and 51.44% respectively.

Furthermore, the following formula was used to calculate the percentage porosity [49]:

$$\% \text{ porosity} = \left[1 - \frac{\rho b}{\rho x}\right] \times 100$$

ρ_b and ρ_x are bulk density and density of x-ray respectively.

The percentage porosity of bare MnO_2, Cs doped-MnO_2 is 16%, and 45% respectively, and upon doping of Sm, the porosity becomes 64%.

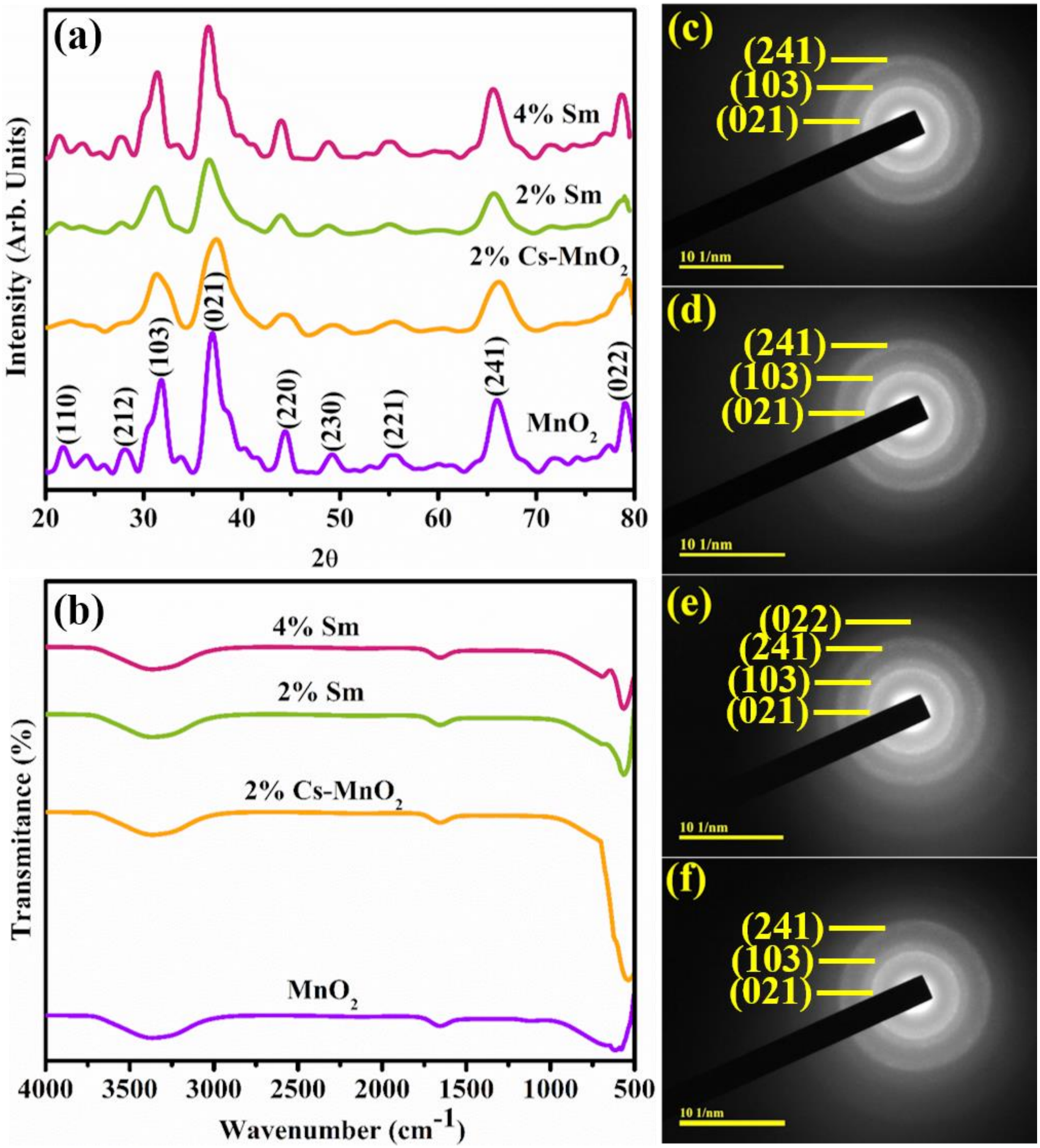

Fig. 2: (a) XRD analysis, (b) FTIR spectra, and (c–f) SAED graphs of MnO_2, Cs-doped MnO_2, and Sm (2 and 4 wt.%)/ Cs-doped MnO_2.

FTIR spectroscopy was used to examine the existence and nature of functional groups, MnO_2, and their chemical functionalities. Fig. 2b depicts the FTIR spectra of bare and Sm/Cs-doped

MnO_2 NSs in the 4000-500 cm^{-1} region. The transmittance range at 1640 cm^{-1} corresponded to the extending oscillations of the adsorbed water molecule, and the stretching vibration of the hydroxyl group was observed in the band at 3300 to 3500 cm^{-1} [50,51]. Pristine MnO_2 is considered high at 584 cm^{-1} [52]. The SAED image (Fig. 2c-f) demonstrates that the MnO_2 as polycrystalline. The circles were observed, aligned to planes (021), (103), (241), and (022), closely inconsistent with XRD data.

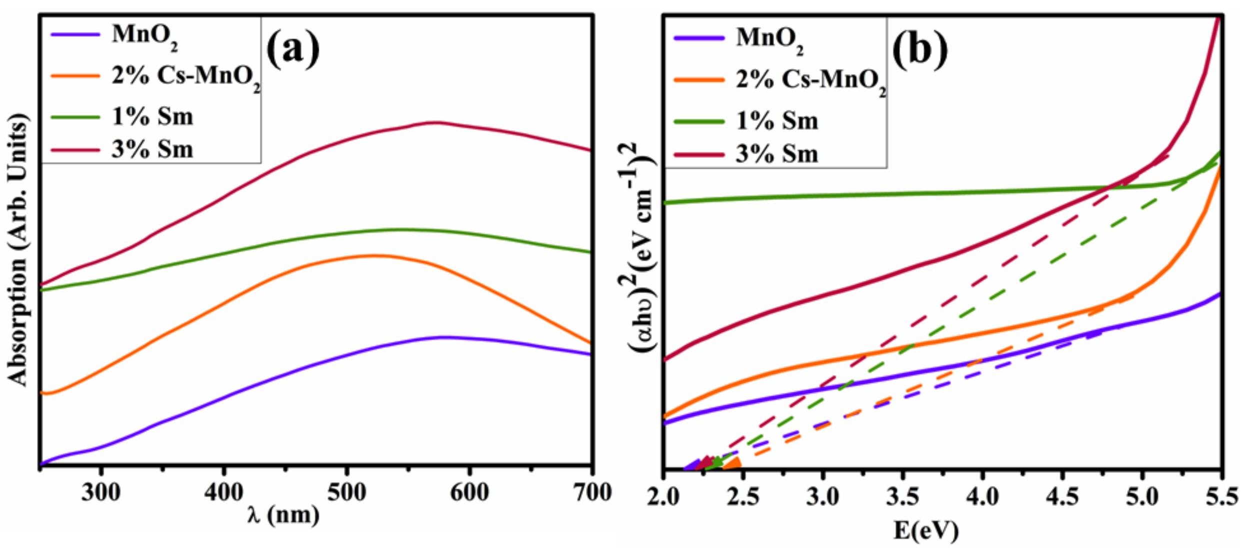

Fig. 3: (a) Absorbance spectra and, (b) band gap energy of MnO_2, Cs-doped MnO_2, and Sm (2 and 4%)/ Cs-doped MnO_2.

The absorption properties of pristine and Sm/Cs doped-MnO_2 NSs were characterized using UV-vis spectroscopy, as elaborated in Fig. 3a. A broad absorption peak for MnO_2 was examined at 580 nm [53]. Absorption spectra shifted towards the blue region with Cs and Sm doping as the absorption range expanded towards a shorter wavelength attributed to π-π* electronic transition

[54]. Energy gaps in the optical spectrum were calculated using the Tauc plot. After doping, the measured Eg of MnO_2 reduced from 2.13 eV to 2.37, 2.27, and 2.19 eV, respectively (Fig. 3b) [55]. Increasing concentration of Sm enhanced E_g manifested to changes in surface structure [56]. Other researchers reported such an increasing band gap with a higher Sm concentration [57–59].

As determined by EDS, Fig. S1 depicts the chemical composition of prepared specimens. The significant spikes of Mn and O affirmed the existence of MnO_2 NSs. The Sm peak is ascribed to the doping of Sm, while the sodium (Na) spike resulted in NaOH to sustain the sample's pH. The potassium (K) high was observed as a precursor $KMnO_4$ used to synthesize MnO_2. Au peaks in spectra were attributed to the coating sprayed onto the samples to decrease the charging effects.

The topography and micro-structure of pristine and doped MnO_2 were confirmed by TEM (Fig. 4a-d). Long Burr-like morphology of undoped MnO_2 revealed as shown in Fig. 4a. Incorporation of Cs demonstrated that long burrs combined, which led to the formation of the aggregated cluster as explained in Fig. 4b. Addition of Sm showed that agglomerated cluster dispersed (Fig. 4c) and higher concentration of Sm determined the disruption of long burrs as illustrated in Fig. 4d.

HR-TEM photographs were adapted to determine inter-planner d-spacing, as indicated in Fig. S2. The d-spacing was calculated as 0.40 nm for MnO_2, allot the plane as (110). Furthermore, the interlayer d-spacing for Cs-doped MnO_2, and (2 and 4%) Sm/Cs-doped MnO_2 were 0.25, 0.17, and 0.13 nm, respectively.

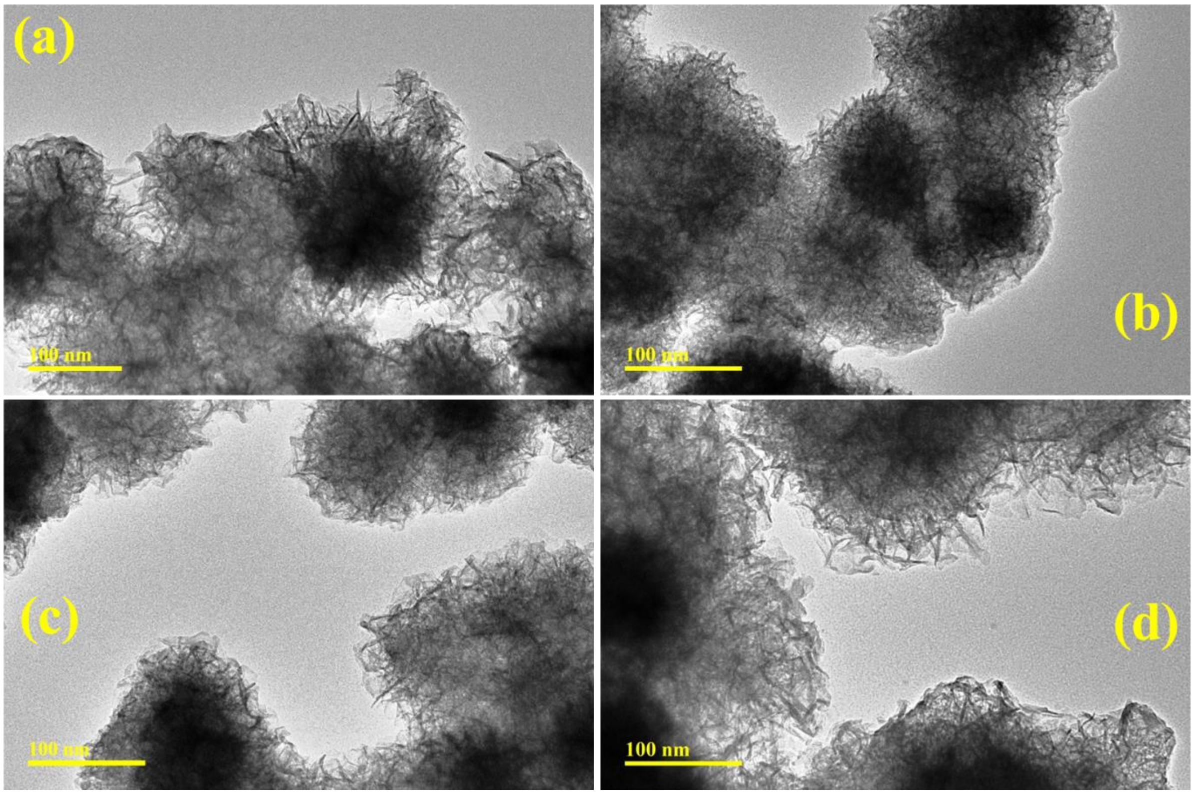

Fig. 4: TEM images of (a) MnO_2 (b) Cs-doped MnO_2, and (c-d) (2 and 4%) Sm/Cs-doped MnO_2.

The reducing agent ($NaBH_4$), oxidizing agent (RhB dye), and catalysts (Sm/Cs doped-MnO_2) were the main components of the catalytic process. Notably, the decolorization of RhB in the presence of $NaBH_4$ progressed slowly. In general, catalysts accelerate the reactions in ongoing research work, elaborated in Fig. S3. However, using the proper catalyst concentration is essential for the dye decolorization experiment. The reduction process initiates with transferring BH^{4-} ions from $NaBH_4$ to RhB molecules dissolved in an aqueous solution to the surface of Sm/Cs-doped MnO_2. The nanocatalysts (NCs) serve as an electron relay system, accelerating the transfer of electrons from the donor to the acceptor and RhB decolorized into leucorhodamine RhB (LRhB). NSs increase the adsorption of BH_4^- ions and dye molecules, whereas an increase in the number of interacting areas promotes rapid interaction between them, leading to efficient dye decomposition [60].

The catalytic activity of undoped and (2 and 4%) Sm/Cs-doped MnO_2 NSs with $NaBH_4$ for the reduction of RhB was investigated using a UV-vis spectrometer (Fig. 5). The pH of the solution and the prepared NCs in RhB dye released at a range of pH levels, influence the degradation rate. All synthesized samples exhibited maximum degradation of 71.42, 71.28, 74.42, and 78% in acidic (pH = 2.5) and 76.42, 75.71, 74.12, and 75.57% in basic (pH = 12), 79.33, 82.44, 87.22 and 91% in neutral (pH = 7) media. In contrast to the alkaline medium, both acidic and neutral environments showed the highest RhB reduction. The degradation seemed to be higher at pH=7; this might be owing to RhB exists in two primary forms in water, zwitter ionic ($RhB^{\pm}$) and cationic (RhB^{+}). As a consequence, in an acid or alkaline solution, both the dye and the catalyst exhibited electrostatic repulsion, and the catalytic efficacies of the Sm/Cs-doped MnO_2 were lower than in a neutral environment [61]. In an acidic environment, maximum degradation efficiency was ascribed to the H^{+} ions production [62]. After incorporating Cs, catalytic efficiency increased in all mediums attributed to the surface area was effectively increased for reaction [63]. In all media, the integration of 4% Sm had the highest degradation rate as it increased oxygen storage capacity [64].

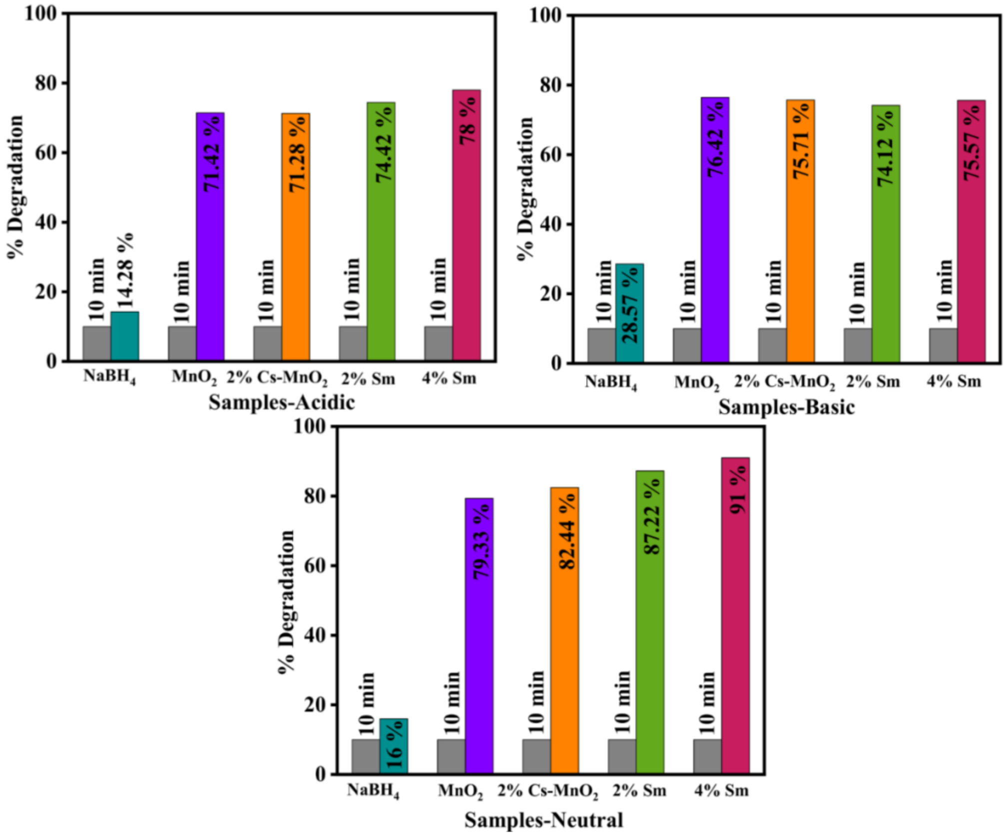

Fig. 5 Catalytic activity of MnO_2, Cs-doped MnO_2, and Sm (2 and 4 wt. %)/Cs-doped MnO_2 NSs in (a) acidic (b) alkaline, and (c) neutral media.

Table 1 Microbicidal efficacy of MnO_2 and Sm/Cs doped-MnO_2 NSs

Samples	Inhibition areas (mm)	
	500 µg/50 µL	1000 µg/50 µL
MnO_2	1.05	1.95
2% Cs- MnO_2	1.35	2.15

2% Sm	1.65	2.55
4% Sm	2.25	2.85
Positive standard	4.95	4.95
Negative standard	0	0

Well-diffusion method was employed to evaluate the bactericidal efficacy of pristine and Sm/CS doped-MnO_2, through the measurement of inhibition zones againt *E. coli*, as depicted in Table 1. *E. coli* inhibition zones were from 1.05–2.25 mm and 1.95–2.85 mm for low and high dosage concentrations, respectively. The inhibition zones were compared to ciprofloxacin (positive control), with an inhibition diameter of 4.95 mm, and DI water (negative control) with 0 mm zone. Pure MnO_2 was less effective against *E. coli* than Sm/Cs-doped MnO_2. The increase in bactericidal potential was observed after the integration of Cs ascribed to the enormous surface area of CS [63]. The antibacterial activity of MnO_2 NSs doped with Sm^{3+} was higher than undoped MnO_2, owing to the presence of oxygen vacancies [65].

Bactericidal action is associated with decreased cell membrane integrity, the formation of free radicals, and the generation of ROS (O^{2-}, HO_2, OH, and H_2O_2) [66,67]. Electron-donating properties of metal oxide produce ROS. Owing to the nanoscale-sized porous membrane of a microbial, nanomaterial with a strong charge and size can damage the membrane. These nanoparticles cause DNA and protein damage, disrupting cell function and eventually destroying cell performance (Fig. S4) [68].

Numerous studies have examined the bactericidal potential of nanoparticles containing metal ions [69–71]. The potential of nanoparticles for interaction with microorganisms through electrostatic, van der Waals, or hydrophobic properties is crucial to their microbicidal activity [72]. Enzymes from several metabolic processes required by microbial cells have been identified as significant candidates for antimicrobials development. Here we assess the inhibitory potential of Cs-doped MnO_2 and Cs/Sm-doped MnO_2 against *E. coli* DNA gyrase and FabB, enzymes from nucleic acid and fatty acid biosynthetic pathway.

Cs-doped MnO_2 has the most favorably docked shape in the functional domain of DNA Gyrase $B_{E.\ coli}$, exhibiting an H-bond interaction with K103, L115, and G117 with a docking score of 3.05. Conversely, Cs/Sm doped MnO_2 (binding score 5.39) formed an H-bond with K103, as seen in Fig. 6b.

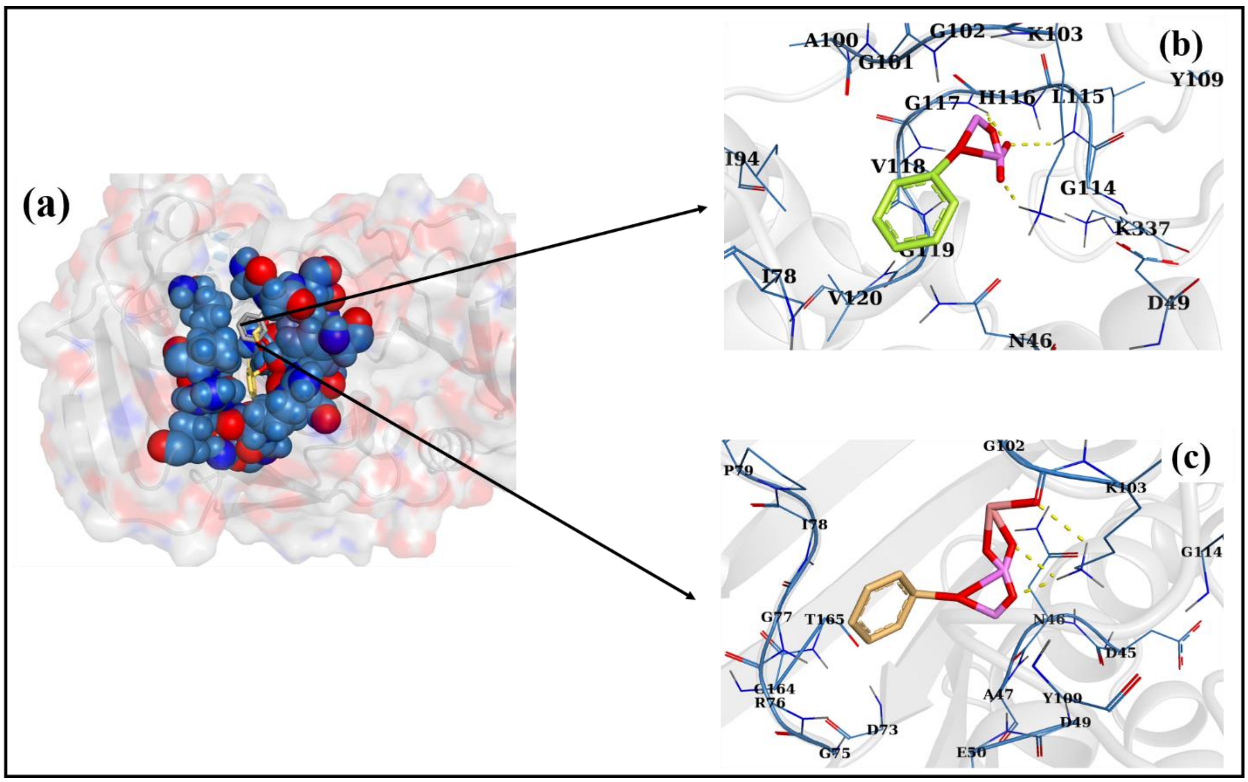

Fig. 6 (a). Nanocomposites-DNA gyrase$_{E.coli}$ docked complexes (superimposed), (b). Cs-doped MnO_2-DNA gyrase$_{E.coli}$ complex, (c). Cs/Sm doped MnO_2-DNA gyrase$_{E.coli}$ complex

The binding potential of these nanorods against $FabB_{E.\ coli}$ was also shown. It was demonstrated that Cs-doped MnO_2 forms H-bonded interactions with T300, T302, V304, and G305, with a cumulative binding score of 1.97. For Cs/Sm doped, MnO_2 docked within the active pocket of

FabB$_{E.\ Coli}$, the best binding score was 4.67, indicating a similar trend. As shown in Fig. 7b, amino acid residues such as T300 and T302 were implicated in H-bond interactions.

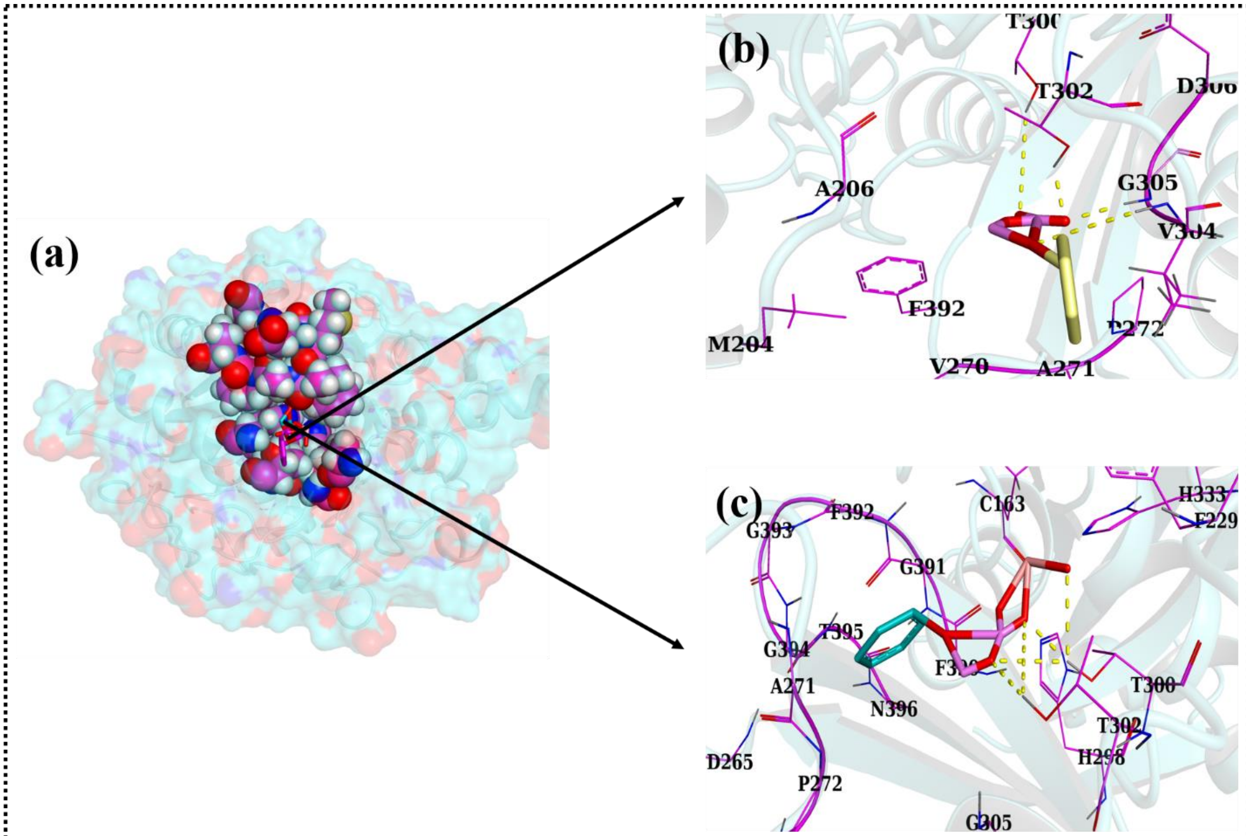

Fig. 7 (a). Nanocomposites FabB$_{E.coli}$ docked complexes (superimposed), (b). Cs-doped MnO_2-FabB$_{E.coli}$ complex, (c). Cs/Sm doped MnO_2-FabB $_{E.coli}$ complex

4. CONCLUSION

In this research, dopant-free and Sm/Cs doped-MnO_2 NSs were produced successfully to improve catalytic and bactericidal activity. Among all prepared samples, Sm/Cs doped-MnO_2 with 4% concentration exhibited effective antimicrobial and catalytic activity at 2.85 and 91%, respectively. FTIR revealed a significant band at 584 cm^{-1} for MnO_2 NSs. Burr-like morphology of MnO_2 NSs was observed, and the optical properties and band gap (2.13, 2.37, 2.27, and 2.17 eV) were calculated through a UV-vis spectrophotometer. In conclusion, Sm/Cs doped-MnO_2 NSs were expressed to be effective against infections and catalytic dye decomposition while also being inexpensive and ecologically benign. Cs/Sm doped MnO_2 was proposed as a potential blocker of FabB and DNA gyrase enzymes in vitro experiments.

Acknowledgment: Authors are thankful to HEC, Pakistan 20-17615 and authors express their appreciation to the Deanship of Scientific Research at King Khalid University, Saudi Arabia, for funding this work through research group program under grant number RGP. 2/428/44.

Conflict of Interest: The authors declare "no conflict of interest."

Data availability statement: On demand

REFERENCES

[1] R.H. Waghchaure, V.A. Adole, B.S. Jagdale, Photocatalytic degradation of methylene blue, rhodamine B, methyl orange and Eriochrome black T dyes by modified ZnO nanocatalysts: A concise review, Inorg. Chem. Commun. 143 (2022). https://doi.org/10.1016/j.inoche.2022.109764.

[2] M. Zhang, C. Zhang, X. Zhai, F. Luo, Y. Du, C. Yan, Antibacterial mechanism and activity of cerium oxide nanoparticles, Sci. China Mater. 62 (2019) 1727–1739. https://doi.org/10.1007/s40843-019-9471-7.

[3] V. Shah, S. Shah, H. Shah, F.J. Rispoli, K.T. McDonnell, S. Workeneh, A. Karakoti, A. Kumar, S. Seal, Antibacterial Activity of Polymer Coated Cerium Oxide Nanoparticles, PLoS One. 7 (2012). https://doi.org/10.1371/journal.pone.0047827.

[4] M. Aadil, A. Rahman, S. Zulfiqar, I.A. Alsafari, M. Shahid, I. Shakir, P.O. Agboola, S. Haider, M.F. Warsi, Facile synthesis of binary metal substituted copper oxide as a solar

light driven photocatalyst and antibacterial substitute, Adv. Powder Technol. 32 (2021) 940–950. https://doi.org/10.1016/j.apt.2021.01.040.

[5] M. Aadil, M. Mahmood, M.F. Warsi, I.A. Alsafari, S. Zulfiqar, M. Shahid, Fabrication of MnO2 nanowires and their nanohybrid with flat conductive matrix for the treatment of industrial effluents, FlatChem. 30 (2021) 100316. https://doi.org/10.1016/j.flatc.2021.100316.

[6] M.S. Lucas, J.A. Peres, Decolorization of the azo dye Reactive Black 5 by Fenton and photo-Fenton oxidation, Dye. Pigment. 71 (2006) 236–244. https://doi.org/10.1016/j.dyepig.2005.07.007.

[7] Y. Dong, K. He, B. Zhao, Y. Yin, L. Yin, A. Zhang, Catalytic ozonation of azo dye active brilliant red X-3B in water with natural mineral brucite, Catal. Commun. 8 (2007) 1599–1603. https://doi.org/10.1016/j.catcom.2007.01.016.

[8] Y. Liu, X. Chen, J. Li, C. Burda, Photocatalytic degradation of azo dyes by nitrogen-doped TiO2 nanocatalysts, Chemosphere. 61 (2005) 11–18. https://doi.org/10.1016/j.chemosphere.2005.03.069.

[9] A. Aguedach, S. Brosillon, J. Morvan, E.K. Lhadi, Photocatalytic degradation of azo-dyes reactive black 5 and reactive yellow 145 in water over a newly deposited titanium dioxide, Appl. Catal. B Environ. 57 (2005) 55–62. https://doi.org/10.1016/j.apcatb.2004.10.009.

[10] A. Rahman, M. Aadil, S. Zulfiqar, I.A. Alsafari, M. Shahid, P.O. Agboola, M.F. Warsi, M.E.F. Abdel-Haliem, Fabrication of binary metal substituted CdO with superior aptitude for dye degradation and antibacterial activity, Ceram. Int. 47 (2021) 8082–8093. https://doi.org/10.1016/j.ceramint.2020.11.163.

[11] J. Hassan, M. Ikram, A. Ul-Hamid, M. Imran, M. Aqeel, S. Ali, Application of Chemically Exfoliated Boron Nitride Nanosheets Doped with Co to Remove Organic Pollutants Rapidly from Textile Water, Nanoscale Res. Lett. 15 (2020). https://doi.org/10.1186/s11671-020-03315-y.

[12] M. Ikram, J. Hassan, A. Raza, A. Haider, S. Naz, A. Ul-Hamid, J. Haider, I. Shahzadi, U. Qamar, S. Ali, Photocatalytic and bactericidal properties and molecular docking analysis of TiO2nanoparticles conjugated with Zr for environmental remediation, RSC Adv. 10 (2020) 30007–30024. https://doi.org/10.1039/d0ra05862a.

[13] Z. Yin, B. Chen, M. Bosman, X. Cao, J. Chen, B. Zheng, H. Zhang, Au nanoparticle-modified MoS2 nanosheet-based photoelectrochemical cells for water splitting, Small. 10 (2014) 3537–3543. https://doi.org/10.1002/smll.201400124.

[14] M.H. Cho, J. Ju, S.J. Kim, H. Jang, Tribological properties of solid lubricants (graphite, Sb2S3, MoS2) for automotive brake friction materials, Wear. 260 (2006) 855–860. https://doi.org/10.1016/j.wear.2005.04.003.

[15] H. Salomon, C. Vignaud, S. Lahlil, N. Menguy, Solutrean and Magdalenian ferruginous rocks heat-treatment: Accidental and/or deliberate action?, J. Archaeol. Sci. 55 (2015) 100–112. https://doi.org/10.1016/j.jas.2014.12.024.

[16] S.Y. Chen, W. Song, H.J. Lin, S. Wang, S. Biswas, M. Mollahosseini, C.H. Kuo, P.X. Gao, S.L. Suib, Manganese Oxide Nanoarray-Based Monolithic Catalysts: Tunable Morphology and High Efficiency for CO Oxidation, ACS Appl. Mater. Interfaces. 8 (2016) 7834–7842. https://doi.org/10.1021/acsami.6b00578.

[17] M.F. Warsi, K. Chaudhary, S. Zulfiqar, A. Rahman, I.A. Al Safari, H.M. Zeeshan, P.O.

Agboola, M. Shahid, M. Suleman, Copper and silver substituted MnO2 nanostructures with superior photocatalytic and antimicrobial activity, Ceram. Int. 48 (2022) 4930–4939. https://doi.org/10.1016/j.ceramint.2021.11.031.

[18] T.D. Dang, A.N. Banerjee, Q.T. Tran, S. Roy, Fast degradation of dyes in water using manganese-oxide-coated diatomite for environmental remediation, J. Phys. Chem. Solids. 98 (2016) 50–58. https://doi.org/10.1016/j.jpcs.2016.06.006.

[19] N.A. Fathy, S.E. El-Shafey, O.I. El-Shafey, W.S. Mohamed, Oxidative degradation of RB19 dye by a novel γ-MnO2/MWCNT nanocomposite catalyst with H2O2, J. Environ. Chem. Eng. 1 (2013) 858–864. https://doi.org/10.1016/j.jece.2013.07.028.

[20] P. Franco, O. Sacco, I. De Marco, D. Sannino, V. Vaiano, Photocatalytic Degradation of Eriochrome Black-T Azo Dye Using Eu-Doped ZnO Prepared by Supercritical Antisolvent Precipitation Route: A Preliminary Investigation, Top. Catal. 63 (2020) 1193–1205. https://doi.org/10.1007/s11244-020-01279-y.

[21] R. Li, J. Yang, S. Xu, Y. Zhou, X. Wang, H. Peng, J. Du, Preparation of Gd-doped TiO2 nanotube arrays by anodization method and its photocatalytic activity for methyl orange degradation, Catalysts. 10 (2020). https://doi.org/10.3390/catal10030298.

[22] K.A. Malik, J.H. Malik, A.A. Bhat, I. Assadullah, R. Tomar, Trap assisted visible light luminescent properties of hydrothermally grown Gd doped ZnO nanostructures, Vacuum. 183 (2021). https://doi.org/10.1016/j.vacuum.2020.109832.

[23] S. Selvaraj, S. Patrick D, G.A. Vangari, M.K. Mohan, P. S, M. C, Facile synthesis of Sm doped ZnO nanoflowers by Co-precipitation method for enhanced photocatalytic degradation of MB dye under sunlight irradiation, Ceram. Int. 48 (2022) 29049–29058.

https://doi.org/10.1016/j.ceramint.2022.04.299.

[24] M.T. Ramesan, T. Sampreeth, In situ synthesis of polyaniline/Sm-doped TiO2 nanocomposites: evaluation of structural, morphological, conductivity studies and gas sensing applications, J. Mater. Sci. Mater. Electron. 29 (2018) 4301–4311. https://doi.org/10.1007/s10854-017-8377-1.

[25] J. Dou, S. Yin, J.Y. Chong, B. Zhang, J. Han, Y. Huang, R. Xu, Carbon spheres anchored Co3O4 nanoclusters as an efficient catalyst for dye degradation, Appl. Catal. A Gen. 513 (2016) 106–115. https://doi.org/10.1016/j.apcata.2015.12.028.

[26] M. Aamir, I. Bibi, S. Ata, F. Majid, S. Kamal, N. Alwadai, M. Sultan, S. Iqbal, M. Aadil, M. Iqbal, Graphene oxide nanocomposite with Co and Fe doped LaCrO3 perovskite active under solar light irradiation for the enhanced degradation of crystal violet dye, J. Mol. Liq. 322 (2021). https://doi.org/10.1016/j.molliq.2020.114895.

[27] Bergey's Manual of Systematics of Archaea and Bacteria, Wiley, 2015. https://doi.org/10.1002/9781118960608.

[28] A.W. Bauer, W.M. Kirby, J.C. Sherris, M. Turck, Antibiotic susceptibility testing by a standardized single disk method., Am. J. Clin. Pathol. 45 (1966) 493–496. https://doi.org/10.1093/ajcp/45.4_ts.493.

[29] F. Adzitey, S. Yussif, R. Ayamga, S. Zuberu, F. Addy, G. Adu-Bonsu, N. Huda, R. Kobun, Antimicrobial Susceptibility and Molecular Characterization of Escherichia coli Recovered from Milk and Related Samples, Microorganisms. 10 (2022). https://doi.org/10.3390/microorganisms10071335.

[30] Wayne PA, Performance standards for antimicrobial susceptibility testing., Clin. Lab. Stand. Inst. 24th Inter (2014) 1–182. https://cir.nii.ac.jp/crid/1130855721503969931 (accessed April 8, 2023).

[31] B.A. Iwalokun, A. Ogunledun, D.O. Ogbolu, S.B. Bamiro, J. Jimi-Omojola, In vitro antimicrobial properties of aqueous garlic extract against multidrug-resistant bacteria and Candida species from Nigeria, J. Med. Food. 7 (2004) 327–333. https://doi.org/10.1089/jmf.2004.7.327.

[32] A. Haider, M. Ijaz, M. Imran, M. Naz, H. Majeed, J.A. Khan, M.M. Ali, M. Ikram, Enhanced bactericidal action and dye degradation of spicy roots' extract-incorporated fine-tuned metal oxide nanoparticles, Appl. Nanosci. 10 (2020) 1095–1104. https://doi.org/10.1007/s13204-019-01188-x.

[33] A. Haider, M. Ijaz, S. Ali, J. Haider, M. Imran, H. Majeed, I. Shahzadi, M.M. Ali, J.A. Khan, M. Ikram, Green Synthesized Phytochemically (Zingiber officinale and Allium sativum) Reduced Nickel Oxide Nanoparticles Confirmed Bactericidal and Catalytic Potential, Nanoscale Res. Lett. 15 (2020). https://doi.org/10.1186/s11671-020-3283-5.

[34] H.Q. Li, L. Shi, Q.S. Li, P.G. Liu, Y. Luo, J. Zhao, H.L. Zhu, Synthesis of C(7) modified chrysin derivatives designing to inhibit β-ketoacyl-acyl carrier protein synthase III (FabH) as antibiotics, Bioorganic Med. Chem. 17 (2009) 6264–6269. https://doi.org/10.1016/j.bmc.2009.07.046.

[35] Z. Mehmood, M. Ikram, M. Imran, A. Shahzadi, A. Haider, A. Ul-Hamid, W. Nabgan, J. Haider, S. Hayat, Z. officinale-doped silver/calcium oxide nanocomposites: Catalytic activity and antimicrobial potential with molecular docking analysis, Process Biochem.

121 (2022) 635–646. https://doi.org/10.1016/j.procbio.2022.07.035.

[36] N.L.S. Lee, K.Y. Yuen, C.R. Kumana, β-Lactam antibiotic and β-lactamase inhibitor combinations, JAMA. 285 (2001) 386–388. https://doi.org/10.1001/jama.285.4.386.

[37] F. V. Stanger, C. Dehio, T. Schirmer, Structure of the N-Terminal Gyrase B fragment in complex with ADP?Pi reveals rigid-body motion induced by ATP hydrolysis, PLoS One. 9 (2014). https://doi.org/10.1371/journal.pone.0107289.

[38] A.C. Price, K.H. Choi, R.J. Heath, Z. Li, S.W. White, C.O. Rock, Inhibition of β-ketoacyl-acyl carrier protein synthases by thiolactomycin and cerulenin: Structure and mechanism, J. Biol. Chem. 276 (2001) 6551–6559. https://doi.org/10.1074/jbc.M007101200.

[39] A. Ul-Hamid, H. Dafalla, A.S. Hakeem, A. Haider, M. Ikram, In-Vitro Catalytic and Antibacterial Potential of Green Synthesized CuO Nanoparticles against Prevalent Multiple Drug Resistant Bovine Mastitogen Staphylococcus aureus, Int. J. Mol. Sci. 23 (2022). https://doi.org/10.3390/ijms23042335.

[40] I. Shahzadi, M. Islam, H. Saeed, A. Haider, A. Shahzadi, J. Haider, N. Ahmed, A. Ul-Hamid, W. Nabgan, M. Ikram, H.A. Rathore, Formation of biocompatible MgO/cellulose grafted hydrogel for efficient bactericidal and controlled release of doxorubicin, Int. J. Biol. Macromol. 220 (2022) 1277–1286. https://doi.org/10.1016/j.ijbiomac.2022.08.142.

[41] M. Ikram, K. Chaudhary, A. Shahzadi, A. Haider, I. Shahzadi, A. Ul-Hamid, N. Abid, J. Haider, W. Nabgan, A.R. Butt, Chitosan/starch-doped MnO2 nanocomposite served as dye degradation, bacterial activity, and insilico molecular docking study, Mater. Today Nano. 20 (2022). https://doi.org/10.1016/j.mtnano.2022.100271.

[42] A. Faisal, A. Abadi, A.D. Faisal, A.A. Aljubouri, Synthesis and Production of Carbon Nanospheres Using Noncatalytic CVD Method, Int. J. Adv. Mater. Res. 2 (2016) 86–91. https://www.researchgate.net/profile/Ali-Abadi/publication/313105476_Synthesis_and_Production_of_Carbon_Nanospheres_Using_Noncatalytic_CVD_Method/links/58904ce192851c9794c66973/Synthesis-and-Production-of-Carbon-Nanospheres-Using-Noncatalytic-CVD-Method.p (accessed April 8, 2023).

[43] M. Faraz, F.K. Naqvi, M. Shakir, N. Khare, Synthesis of samarium-doped zinc oxide nanoparticles with improved photocatalytic performance and recyclability under visible light irradiation, New J. Chem. 42 (2018) 2295–2305. https://doi.org/10.1039/c7nj03927a.

[44] M. Wang, J. Han, P. Guo, M. Sun, Y. Zhang, Z. Tong, M. You, C. Lv, Hydrothermal synthesis of B-doped Bi2MoO6 and its high photocatalytic performance for the degradation of Rhodamine B, J. Phys. Chem. Solids. 113 (2018) 86–93. https://doi.org/10.1016/j.jpcs.2017.10.019.

[45] M. Aadil, A.G. Taki, S. Zulfiqar, A. Rahman, M. Shahid, M.F. Warsi, Z. Ahmad, A.A. Alothman, S. Mohammad, Gadolinium doped zinc ferrite nanoarchitecture reinforced with a carbonaceous matrix: a novel hybrid material for next-generation flexible capacitors, RSC Adv. 13 (2023) 28063–28075. https://doi.org/10.1039/d3ra05290g.

[46] M. Rashid, W. Hassan, M. Aadil, H.H. Somaily, N.M. Mahdi, R. Lataef, A.G. Taki, K. Srithilat, D.F. Baamer, S.M. Albukhari, M.A. Salam, A. Llyas, Solar-light-driven and magnetically recoverable doped nano-ferrite: An ideal photocatalyst for water purification applications, Opt. Mater. (Amst). 135 (2023).

https://doi.org/10.1016/j.optmat.2022.113192.

[47] S. Majumdar, The effects of crystallite size, surface area and morphology on the sensing properties of nanocrystalline SnO2 based system, Ceram. Int. 41 (2015) 14350–14358. https://doi.org/10.1016/j.ceramint.2015.07.068.

[48] Y.S. Danilov, Effect of grain size on the Bauschinger effect, Met. Sci. Heat Treat. 6 (1964) 563–565. https://doi.org/10.1007/BF00652409.

[49] M. Aadil, W. Hassan, H.H. Somaily, S.R. Ejaz, R.R. Abass, H. Jasem, S.K. Hachim, A.H. Adhab, E.S. Abood, I.A. Alsafari, Synergistic effect of doping and nanotechnology to fabricate highly efficient photocatalyst for environmental remediation, J. Alloys Compd. 920 (2022). https://doi.org/10.1016/j.jallcom.2022.165876.

[50] E. Bartonickova, J. Cihlar, K. Castkova, Microwave-assisted synthesis of bismuth oxide, Process. Appl. Ceram. 1 (2007) 29–33. https://doi.org/10.2298/pac0702029b.

[51] W. Raza, M.M. Haque, M. Muneer, T. Harada, M. Matsumura, Synthesis, characterization and photocatalytic performance of visible light induced bismuth oxide nanoparticle, J. Alloys Compd. 648 (2015) 641–650. https://doi.org/10.1016/j.jallcom.2015.06.245.

[52] K. Rout, M. Mohapatra, S. Anand, A critical analysis of cation adsorption from single and binary solutions on low surface area β-MnO 2, Appl. Surf. Sci. 270 (2013) 205–218. https://doi.org/10.1016/j.apsusc.2013.01.002.

[53] S. Dhingra, T. Chhabra, V. Krishnan, C.M. Nagaraja, Visible-Light-Driven Selective Oxidation of Biomass-Derived HMF to DFF Coupled with H2Generation by Noble Metal-Free Zn0.5Cd0.5S/MnO2Heterostructures, ACS Appl. Energy Mater. 3 (2020) 7138–

7148. https://doi.org/10.1021/acsaem.0c01189.

[54] K. Skrabania, A. Miasnikova, A.M. Bivigou-Koumba, D. Zehm, A. Laschewsky, Examining the UV-vis absorption of RAFT chain transfer agents and their use for polymer analysis, Polym. Chem. 2 (2011) 2074–2083. https://doi.org/10.1039/c1py00173f.

[55] B.A. Pinaud, Z. Chen, D.N. Abram, T.F. Jaramillo, Thin films of sodium birnessite-type MnO2: Optical properties, electronic band structure, and solar photoelectrochemistry, J. Phys. Chem. C. 115 (2011) 11830–11838. https://doi.org/10.1021/jp200015p.

[56] R. Zamiri, A.F. Lemos, A. Reblo, H.A. Ahangar, J.M.F. Ferreira, Effects of rare-earth (Er, la and Yb) doping on morphology and structure properties of ZnO nanostructures prepared by wet chemical method, Ceram. Int. 40 (2014) 523–529. https://doi.org/10.1016/j.ceramint.2013.06.034.

[57] H.Y. He, J. Fei, J. Lu, Sm-doping effect on optical and electrical properties of ZnO films, J. Nanostructure Chem. 5 (2015) 169–175. https://doi.org/10.1007/s40097-015-0147-0.

[58] P. Velusamy, R.R. Babu, K.T. Aparna, Effect of Sm doping on the physical properties of ZnO thin films deposited by spray pyrolysis technique, in: AIP Conf. Proc., American Institute of Physics Inc., 2017. https://doi.org/10.1063/1.4980545.

[59] M.M. Ba-Abbad, M.S. Takriff, A. Benamor, M.S. Nasser, E. Mahmoudi, A.W. Mohammad, Synthesis and characterization of Sm3+-doped ZnO nanoparticles via a sol–gel method and their photocatalytic application, J. Sol-Gel Sci. Technol. 85 (2018) 178–190. https://doi.org/10.1007/s10971-017-4503-z.

[60] A. Bari, M. Ikram, A. Haider, A. Ul-Hamid, J. Haider, I. Shahzadi, G. Nazir, A. Shahzadi,

M. Imran, A. Ghaffar, Evaluation of bactericidal potential and catalytic dye degradation of multiple morphology based chitosan/polyvinylpyrrolidone-doped bismuth oxide nanostructures, Nanoscale Adv. 4 (2022) 2713–2728. https://doi.org/10.1039/d2na00105e.

[61] Y. Chen, B. Zhai, Y. Liang, Enhanced degradation performance of organic dyes removal by semiconductor/MOF/graphene oxide composites under visible light irradiation, Diam. Relat. Mater. 98 (2019). https://doi.org/10.1016/j.diamond.2019.107508.

[62] A. Rafique, M. Ikram, A. Haider, A. Ul-Hamid, S. Naz, W. Nabgan, J. Haider, I. Shahzadi, Dye degradation, antibacterial activity and molecular docking analysis of cellulose/polyvinylpyrrolidone-doped cadmium sulphide quantum dots, Int. J. Biol. Macromol. 214 (2022) 264–277. https://doi.org/10.1016/j.ijbiomac.2022.06.058.

[63] A.A. Deshmukh, S.D. Mhlanga, N.J. Coville, Carbon spheres, Mater. Sci. Eng. R Reports. 70 (2010) 1–28. https://doi.org/10.1016/j.mser.2010.06.017.

[64] T. Deng, C. Zhang, Y. Xiao, A. Xie, Y. Pang, Y. Yang, One-step synthesis of samarium-doped ceria and its CO catalysis, Bull. Mater. Sci. 38 (2015) 1149–1154. https://doi.org/10.1007/s12034-015-0994-9.

[65] A. Balamurugan, M. Sudha, S. Surendhiran, R. Anandarasu, S. Ravikumar, Y.A. Syed Khadar, Hydrothermal synthesis of samarium (Sm) doped cerium oxide (CeO2) nanoparticles: Characterization and antibacterial activity, in: Mater. Today Proc., 2019: pp. 3588–3594. https://doi.org/10.1016/j.matpr.2019.08.217.

[66] S. Meghana, P. Kabra, S. Chakraborty, N. Padmavathy, Understanding the pathway of antibacterial activity of copper oxide nanoparticles, RSC Adv. 5 (2015) 12293–12299. https://doi.org/10.1039/c4ra12163e.

[67] S. Jadhav, S. Gaikwad, M. Nimse, A. Rajbhoj, Copper Oxide Nanoparticles: Synthesis, Characterization and Their Antibacterial Activity, J. Clust. Sci. 22 (2011) 121–129. https://doi.org/10.1007/s10876-011-0349-7.

[68] C.Z. Chen, S.L. Cooper, Interactions between dendrimer biocides and bacterial membranes, Biomaterials. 23 (2002) 3359–3368. https://doi.org/10.1016/S0142-9612(02)00036-4.

[69] T. Shujah, A. Shahzadi, A. Haider, M. Mustajab, A.M. Haider, A. Ul-Hamid, J. Haider, W. Nabgan, M. Ikram, Molybdenum-doped iron oxide nanostructures synthesized via a chemical co-precipitation route for efficient dye degradation and antimicrobial performance: in silico molecular docking studies, RSC Adv. 12 (2022) 35177–35191. https://doi.org/10.1039/d2ra07238f.

[70] M. Ikram, A. Haider, M. Imran, J. Haider, A. Ul-Hamid, A. Shahzadi, R. Malik, Kashaf-Ul-Ain, W. Nabgan, G. Nazir, S. Ali, Graphitic-C3N4/chitosan-doped NiO nanostructure to treat the polluted water and their bactericidal with in silico molecular docking analysis, Int. J. Biol. Macromol. 227 (2023) 962–973. https://doi.org/10.1016/j.ijbiomac.2022.11.273.

[71] M. Ikram, H. Maghfoor, A. Shahzadi, A. Haider, I. Shahzadi, N. Abid, A. Ul-Hamid, J. Haider, W. Nabgan, A.R. Butt, Towards effective dye degradation and antimicrobial behavior of chitosan and C3N4-doped CdS nanoparticles, Mater. Today Commun. 33 (2022). https://doi.org/10.1016/j.mtcomm.2022.104814.

[72] S. Shaheen, A. Iqbal, M. Ikram, M. Imran, S. Naz, A. Ul-Hamid, A. Shahzadi, W. Nabgan, J. Haider, A. Haider, Graphene oxide-ZnO nanorods for efficient dye

degradation, antibacterial and in-silico analysis, Appl. Nanosci. 12 (2022) 165–177. https://doi.org/10.1007/s13204-021-02251-2.

Catalytic action and bactericidal behavior of samarium/carbon spheres-doped manganese oxide nanostructures and their molecular docking analysis

Ehtasham Ul Haq[a], Muhammad Imran[a], Ali Haider[b], Anum Shahzadi[c], Ayesha Habib[d], Anwar Ul-Hamid[e], Walid Nabgan[f*], Majed A. Bajaber[g], Muhammad Ikram[d*]

[a]Department of Chemistry, Government College University, Faisalabad, Sahiwal Road, Sahiwal, Punjab, 57000, Pakistan
[b]Department of Clinical Sciences, Faculty of Veterinary and Animal Sciences, Muhammad Nawaz Shareef, University of Agriculture, Multan 66000, Punjab, Pakistan
[c]Department of Pharmacy, COMSATS University Islamabad, Lahore Campus, Lahore 54000, Pakistan
[d]Solar Cell Applications Research Lab, Department of Physics, Government College University Lahore, Lahore 54000, Punjab, Pakistan
[e]Core Research Facilities, King Fahd University of Petroleum & Minerals, Dhahran 31261, Saudi Arabia
[f]Departament d'Enginyeria Química, Universitat Rovira i Virgili, Av Països Catalans 26, 43007 Tarragona, Spain
[g]Chemistry Department, Faculty of Science, King Khalid University, P.O. Box 9004, Abha 61413, Saudi Arabia

Corresponding authors email: [d]dr.muhammadikram@gcu.edu.pk, [f]wnabgan@gmail.com

Abstract

The co-precipitation technique was adapted to synthesize different concentrations (2 and 4 %) of samarium (Sm) doped constant equates of carbon spheres (Cs) and manganese oxide (MnO_2). The principal objective of this investigation is to demonstrate confirmation that Sm/Cs-doped MnO_2 nanostructures (NSs) owned antibacterial and catalytic attributes. Reduction in surface area manifested to agglomeration, NSs faces become inaccessible to initiate a reaction, can be overcome upon doping of Sm. Sm has the potential to increase the activity of metal oxide ascribed to its electron trapping effect. The structural morphologies, optical properties, functional groups, elemental composition, and d-spacing were determined by applying various characterizations. With the incorporation of CS and Sm, UV-vis spectra shifted towards lower wavelength and band gap energy (Eg) was reduced. MnO_2 possessed orthorhombic structure, according to the XRD pattern and TEM exhibited long Burr-like morphology of undoped MnO_2. SAED image illustrated that MnO_2 is polycrystalline. 4% Sm/CS doped MnO_2 revealed the highest degradation (91%) in a neutral environment. Furthermore, 4% Sm/Cs doped-MnO_2 revealed an inhibitory zone of 2.85 mm against *Escherichia coli* (*E. coli*). Additionally, an analysis of molecular docking revealed a binding interface with NRs and the functional domains

of certain cellular proteins. Results indicated that Cs-doped MnO_2 and Cs/Sm-doped MnO_2 NRs are the most potent DNA gyrase and FabB enzyme inhibitors.

Keywords: Catalyst, bactericidal, samarium/carbon, molecular docking

INTRODUCTION

In the time of scientific innovation and industrial development, the environment is mainly the victim of industrial by-products. Water pollution is a major environmental problem that gets worse over time. Organic wastes, likely dyes, are the utmost dischargeable impurities in water, which threaten lives. It may cause severe damage to the kidney, liver, and central nervous system (CNS). Dyes, including Rhodamine B (RhB), methyl orange (MO), methylene blue, and congo red, are toxic, with mutagenic and carcinogenic effects on humans and ecosystems [1]. Mastitis incurs significant financial implications for the dairy industry. It's attributed to abnormalities in milk's microbiome, chemistry, physical alterations, and structural modifications to the mammary glandular pad. Pathogens, including *E. coli* and *Staphylococcus aureus* (*S. aureus*), can evolve from various sources like the host, atmosphere, season, and typical pathogen [2,3]. The parasitic microbes reproduce rapidly, eradicating indigenous aquatic species and harming the ecosystem by lowering dissolved oxygen levels [4,5]. Several techniques, such as adsorption, catalysis, advanced oxidation process [6], ozonation [7], irradiation, and photocatalysis [8,9], can be used for wastewater treatment. Several theories have been proposed on the mechanisms behind the influence of metallic nanoparticles (MNPs) on microbial enzymes. These theories include the disruption of microbial enzymes caused by metal ion liberation, changes in membrane integrity resulting in penetration into the bacterial cytoplasm, accumulation within the periplasmic space, and direct influence by reactive oxygen species (ROS) produced as a result of MNP exposure [10]. Catalysis is a cost-effective, environment-friendly, and energy-efficient process [11].

In the last few years, semiconductor nanomaterials (NMs) have aroused considerable interest in environmental development for researchers. Two-dimensional (2D) materials, including MoS_2, BN, GO, MnO_2, and WS_2, are currently being employed to improve water purification [12–14]. MnO_2 is naturally abundant, low toxic, and cheaper [15]. MnO_2 is one of the most attractive inorganic materials owing to its structural and physical characteristics, broad implementations in energy storage, catalysis [15], antimicrobial activity, ion exchange, biosensors, and molecular sieves [16]. However, MnO_2 has a wider bandgap, which limits its ability to absorb visible light. Consequently, several strives have been to improve MnO_2's antibacterial capacity and dye degradation effectiveness[17]. Dang's group synthesized MnO_2-coated diatomite composite via a wet-chemical technique to evaluate the degradation rate of MO and MB [18]. Fathy et al. employed a co-precipitation methodology to prepare MnO_2/MWCNT nanocomposite catalyst and assessed the oxidative decolorization of RB19 dye [19]. To improve the dye degradation, other publications on metal oxides doped with RE metal ions are also published as Eu-doped ZnO [20], Gd-doped TiO_2 [21], Gd-doped ZnO [22], and Sm-doped ZnO [23]. This study focuses on Sm doping in MnO_2 for better Catalytic activity. Sm ions (Sm^{2+} and Sm^{3+}) can potentially upgrade metal oxide activities ascribed to trapping electrons [24]. Carbon spheres are a significant candidate for a novel form of catalytic support because of their abundance of surface functional groups, including carboxylic, hydroxyl, and carbonyl groups. For example, carbon spheres have been employed as a support for the immobilizing of metal oxides, metal sulphides and metals [25]. Modification in MnO_2 optical and catalytic properties with rare earth metal and Carbonaceous spheres has been excepted as an promising methodology for better waste water remediation against RhB, , to the best of our comprehension , no publication has been reported on this.

In this study, reference samples and Sm/Cs doped-MnO_2 NSs have been prepared by co-precipitation approach. Antimicrobial action against *E. coli* and dye removal from water were studied using synthesized samples. The detailed analysis of the ternary system was observed by a variety of characterizations

2 EXPERIMENTAL SECTIONS

2.1 Materials

Manganese (II) sulfate monohydrate ($MnSO_4.H_2O$, 99%, Panreac*)*, Potassium per-manganate ($KMnO_4$, 99.5%, AnalaR), Sodium hydroxide (NaOH, 98%) had received from Sigma-Aldrich. Samarium (III) nitrate hexa-hydrate ($Sm\ (NO_3)_3.6H_2O$, 99.9%, Alfa-Aesar) were used as purchased.

2.2 Synthesis of Cs

The hydrothermal carbonization method was utilized to prepare Cs. A 1 M glucose solution was prepared at continual stirring to attain the desired transparent and straightforward solution. The aqueous solution was autoclaved at 180 ˚C for 12 h. Cs were recovered by washing the accompanied precipitates with DI water and drying them overnight at 100 ˚C, as shown in Fig. 1a.

2.3 Synthesis of MnO_2 and Sm/Cs doped-MnO_2

Co-precipitation was employed to synthesize MnO_2 NSs using 0.5 M of $MnSO_4.H_2O$ and $KMnO_4$, stirred vigorously at 80 ˚C. The pH remained steady at 12 with a dropwise inclusion of

1 M NaOH. The precipitates were washed out by centrifugation twice (7 min at 7000 rpm) under continuous stirring, heated overnight at 150 ˚C, and crushed to obtain MnO_2 fine powder. Similarly, the procedure mentioned above was followed to synthesize distinct concentrations (2 and 4%) of Sm-doped fixed amounts of Cs into MnO_2, as portrayed in Fig. 1b.

2.4 Catalysis

The CA of pristine and Sm/Cs doped-MnO_2 was performed using 400 L of Sodium borohydride ($NaBH_4$) as the reductant and 3 mL of newly prepared MB solution as the oxidant. Consequently, 400 mL of synthesized samples were added to the above solution. Decolorization of RhB into LRhB was observed at predictable spans. The degradation rate was studied by UV-vis spectrophotometer, and the %age of dye degradation was assessed as follows [26]:

$$\% \text{ Degradation} = \frac{C_0 - C_t}{C_o} \times 100 \text{ ------------------- } (1)$$

2.5 Segregation and Identification of MDR *E. coli*

2.5.1 Specimens Assortment

Raw milk samples from selected dairy cattle were collected by direct milking into disinfected glassware marketed at various veterinary hospitals, markets, and farms in Punjab, Pakistan. Plain milk was transferred to the laboratory promptly after being retrieved at 4 ˚C. The coliforms in raw milk were enumerated on MacConkey agar. Plates were incubated for 48 h at 37 ˚C.

2.5.2 Recognition and Differentiation of Bacteria

Gram staining and various biochemical procedures were executed to validate the initial recognition of *E. coli* based on the colony shape seen, as described in Bergey's Manual of Determinative Bacteriology [27].

2.5.3 Antibiotic susceptibility

Disk diffusion was used by Bauer et al. [28] over Mueller Hinton agar to test antibiotic susceptibility (MHA). Antibiotic resistance of *E. coli* was determined by performing a test on the subsequent antibiotics (classes); Tetracycline (Te) 30 µg (Tetracyclines), Amoxycillin (A) 30 µg (Penicillins), Ciprofloxacin (Cip) 5 µg (Quinolones), Gentamicin (Gm) 10 µg (Aminoglycosides), Azithromycin (Azm) 15 µg (Macrolides), Ceftriaxone (Cro) 30 µg (Cephalosporins) and Imipenem (Imi) 10 µg (Carbapenem), [29]. The turbidity of *E. coli* decontaminated colonies was set to 0.5 MacFarland. In addition, the contaminated plates were spread-plated over Muller Hinton Agar (MHA) to avoid the antibiotic plates from overlaying their inhibitory domains. After 24 hours of incubation at 37°C, the findings were interpreted in accordance with the criteria established by the Clinical and Laboratory Standard Institute [30]. Bacteria that showed resistance to at least three different antibiotics were classified as multidrug-resistant [31].

2.5.4 Antibacterial Evaluation

Using agar well diffusion technology, in vitro bactericidal action of pristine and Sm/Cs doped-MnO_2 was assessed by MDR *E. coli* reflective strains collected from mastitis milk. The 0.5 McFarland norm of MDR *E. coli* was swabbed onto Macconkey agar dishes. A septic cork borer was adopted to construct 6 mm diameter holes in agar. Developed materials were employed at both mild (0.5 mg/50 µl) and higher (1.0 mg/50 µl) concentrations. We accordingly employed dilutions of ciprofloxacin (0.005 mg/50 µl) and DI water (50 µl) as positive and negative standards [32].

2.5.5 Statistical analysis

Inhibition region widths (in mm) were used to determine antibacterial efficacy, and single-way variance analysis (ANOVA) employing SPSS 20 was implemented for the statistical evaluation [33].

2.7 Molecular Docking Analysis

Molecular binding investigation of Cs-doped MnO_2 and Cs/Sm-doped MnO_2 was studied. This was done by focusing on integral proteins for microbial progression and maintenance. Binding analysis was subjected to several protein targets from different biosynthetic processes, including DNA gyrase$_{\textit{E. coli}}$ and -ketoacyl- [acyl carrier protein] synthase I. (FabB) B$_{\textit{E. coli}}$. DNA gyrase is critical in producing genetic material and folic acid, essential for microbial resilience. FabB catalyzes critical stages in bacterial cells' fatty acid biosynthesis pathway [34–36]. Crystal structures of *E. coli* target proteins were obtained using a protein data library (Fig. S5). Protein Data Bank was examined for structures of DNA gyrase B$_{\textit{E. coli}}$ (PDB ID: 4PRV), resolution:1.45 [37], and -ketoacyl- [acyl carrier protein] synthase I (FabB) B$_{\textit{E. coli}}$ (PDB ID: 1FJ4),) resolution:2.35 [38]. The binding analysis was performed with SYBYL-X 2.0 software suite [39]. SYBYL-X 2.0 was utilized to create 3D frameworks of compounds and assess the binding capacities of nanorods with the active domain motifs of chosen proteins, the same as it had been employed in our prior studies [40,41].

3 RESULTS AND DISCUSSION

Cs were synthesized using hydrothermal carbonization, illustrated in Fig. 1a. Various Sm concentrations (2 and 4 wt.%) were doped into Cs/MnO_2 via the co-precipitation route, as shown in Fig. 1b.

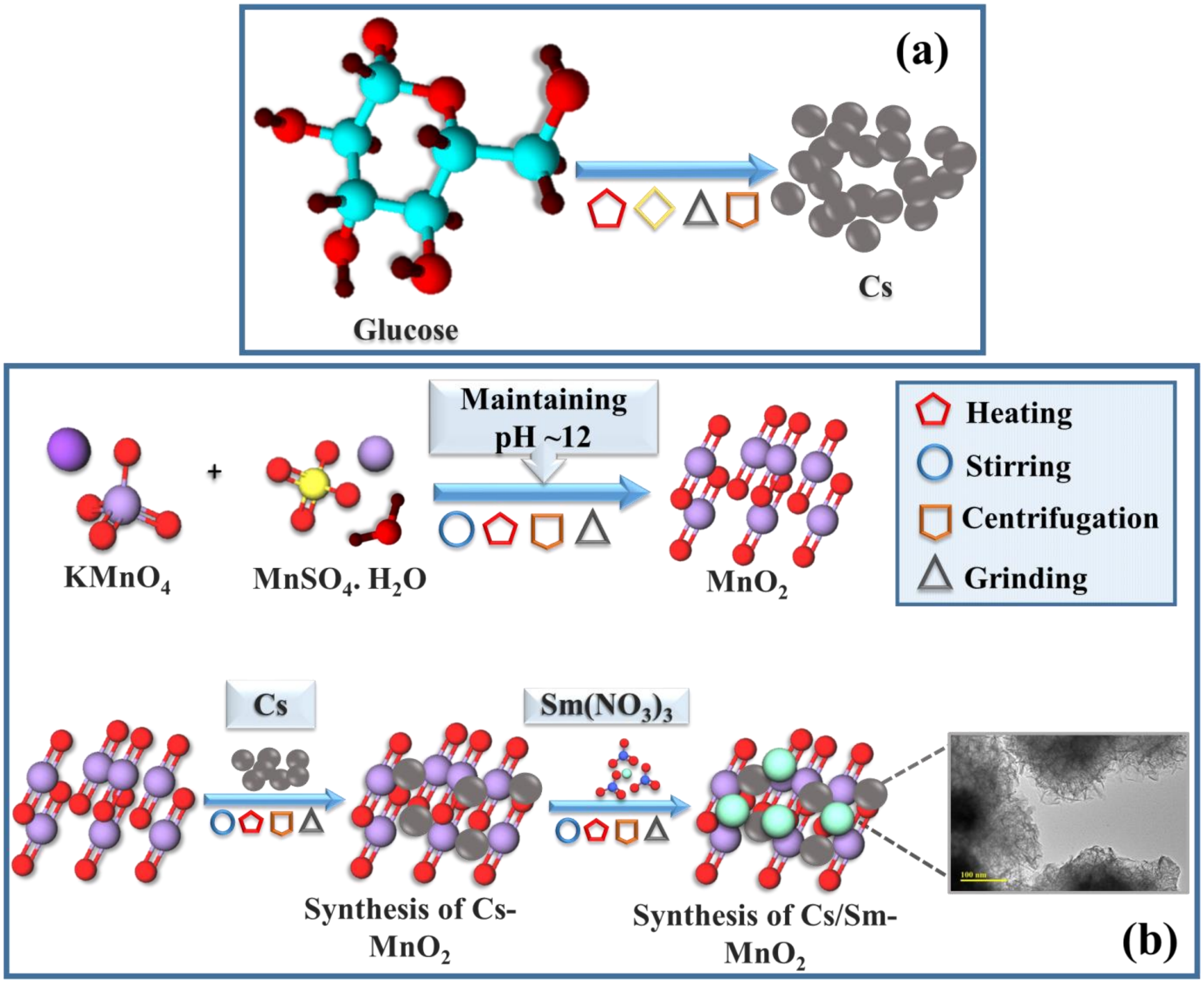

Fig. 1: (a) Schematic synthesis of Cs and (b) integration of Sm/Cs-doped MnO_2.

Fig. 2a illustrates the structural properties and phase purity of MnO_2 and Sm/Cs-doped MnO_2 NSs employing XRD patterns. Bragg Peaks sited at 21.70° (110), 36.95° (021), 44.42° (220), 49.32° (230), 55.36° (221), 66.05° (241), and 79.09° (022) confirmed the orthorhombic structure of MnO_2 by (JCPDF 01-073-1539/00-039-0375). Moreover, peaks at 28.05° (212) and 32.27° (103) attributed to Mn_2O_3 and Mn_2O_4, respectively advocated by (01-073-1826/00-024-0734). Upon doping of Cs, peaks broadening were noticed, attributed to their small crystal size. Peak broadening is also associated with amorphous carbon and low-degree graphitization [42]. The intensity of peaks decreased and broadened upon the incorporation of 2% Sm into MnO_2 as it inhibits the growth of the MnO_2 lattice, in line with earlier reports [43]. However, the higher doping of Sm increased the peak intensity, which implies that Sm integration may be advantageous to the growth of preferential orientation [44]. Using the Debye-Scherer formula calculated the grain (crystallite) size of prepared samples as mentioned below [45]:

$$\text{G.S} = \frac{k\lambda}{\beta Cos\theta}$$

The grain size of MnO_2, Cs doped-MnO_2, and (2 and 4 wt.%)Sm/Cs doped-MnO_2 was measured as 14.60, 12.67, 9.89, and 12.92 nm respectively.

The specimens' surface area was computed using the following equation [46]:

$$\text{Surface area} = \frac{6000}{G.S \times \rho x}$$

The surface area of MnO_2, Cs doped-MnO_2, and (2 and 4 wt. %)Sm/Cs doped-MnO_2 is 96, 97, 156.43, and 119.38 m^2/g.

As crystallite size increases, surface characteristics such as specific surface area and surface-to-volume ratio decrease [47]. In smaller grains, deformation occurs due to changes in the surface state of the boundary [48] which is why surface area increases and vice versa.

The following relationship was used to compute the percentage crystallinity of as-synthesized specimens [49]:

$$\text{\% Crystallinity} = \frac{Area\ under\ the\ crystalline\ peak}{Area\ of\ all\ peaks}$$

The pristine MnO_2, Cs doped-MnO_2, and (2 and 4%)Sm/Cs doped-MnO_2 had a calculated crystallinity of 55.63, 30.34, 29.89, and 51.44% respectively.

Furthermore, the following formula was used to calculate the percentage porosity [49]:

$$\% \text{ porosity} = [1 - \frac{\rho b}{\rho x}] \times 100$$

ρ_b and ρ_x are bulk density and density of x-ray respectively.

The percentage porosity of bare MnO_2, Cs doped-MnO_2 is 16%, and 45% respectively, and upon doping of Sm, the porosity becomes 64%.

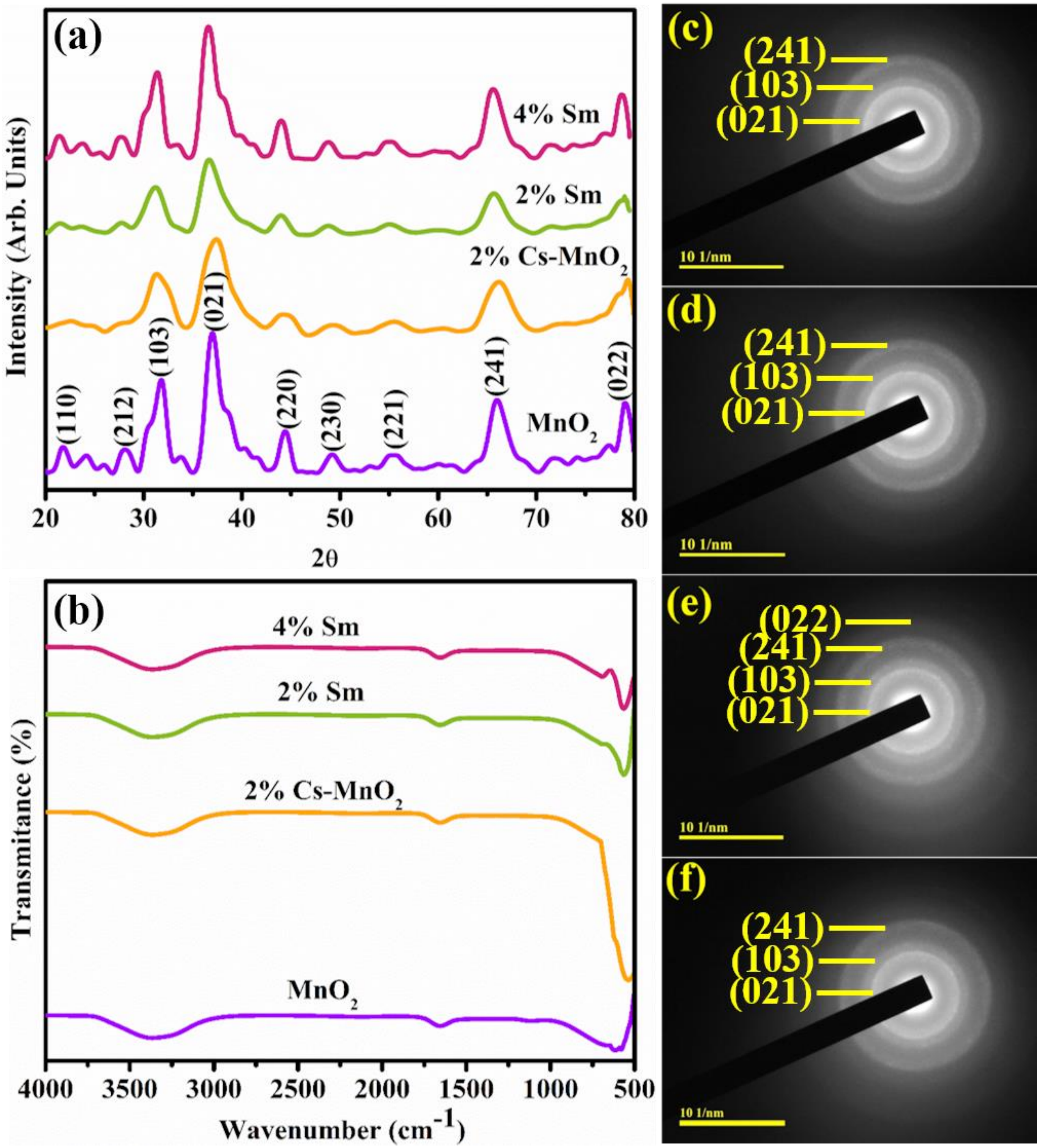

Fig. 2: (a) XRD analysis, (b) FTIR spectra, and (c–f) SAED graphs of MnO_2, Cs-doped MnO_2, and Sm (2 and 4 wt.%)/ Cs-doped MnO_2.

FTIR spectroscopy was used to examine the existence and nature of functional groups, MnO_2, and their chemical functionalities. Fig. 2b depicts the FTIR spectra of bare and Sm/Cs-doped

MnO_2 NSs in the 4000-500 cm^{-1} region. The transmittance range at 1640 cm^{-1} corresponded to the extending oscillations of the adsorbed water molecule, and the stretching vibration of the hydroxyl group was observed in the band at 3300 to 3500 cm^{-1} [50,51]. Pristine MnO_2 is considered high at 584 cm^{-1} [52]. The SAED image (Fig. 2c-f) demonstrates that the MnO_2 as polycrystalline. The circles were observed, aligned to planes (021), (103), (241), and (022), closely inconsistent with XRD data.

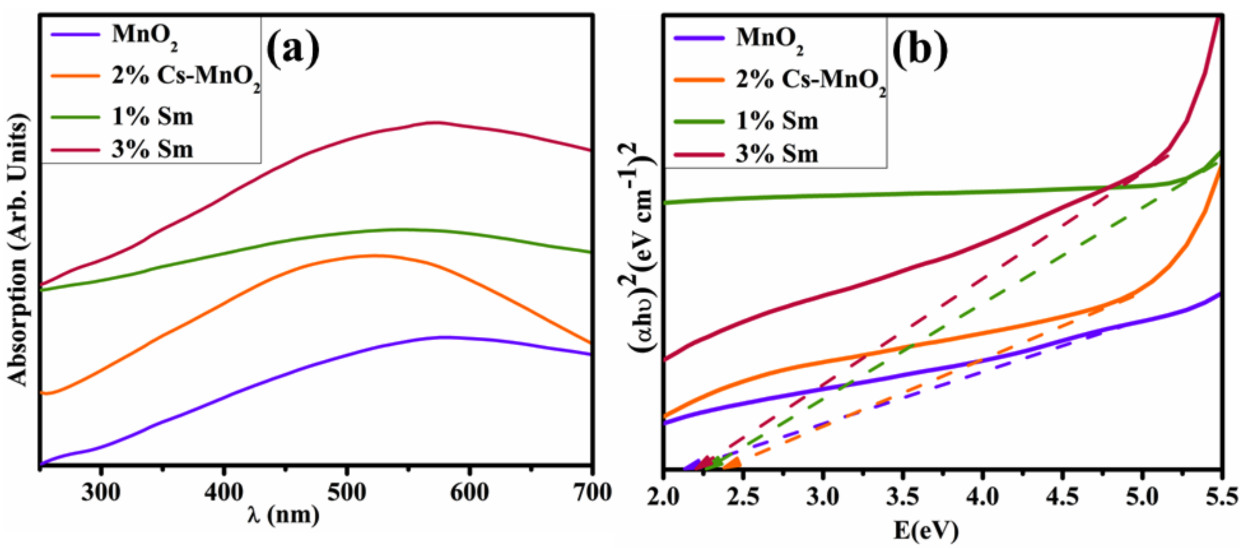

Fig. 3: (a) Absorbance spectra and, (b) band gap energy of MnO_2, Cs-doped MnO_2, and Sm (2 and 4%)/ Cs-doped MnO_2.

The absorption properties of pristine and Sm/Cs doped-MnO_2 NSs were characterized using UV-vis spectroscopy, as elaborated in Fig. 3a. A broad absorption peak for MnO_2 was examined at 580 nm [53]. Absorption spectra shifted towards the blue region with Cs and Sm doping as the absorption range expanded towards a shorter wavelength attributed to π-π* electronic transition

[54]. Energy gaps in the optical spectrum were calculated using the Tauc plot. After doping, the measured Eg of MnO_2 reduced from 2.13 eV to 2.37, 2.27, and 2.19 eV, respectively (Fig. 3b) [55]. Increasing concentration of Sm enhanced E_g manifested to changes in surface structure [56]. Other researchers reported such an increasing band gap with a higher Sm concentration [57–59].

As determined by EDS, Fig. S1 depicts the chemical composition of prepared specimens. The significant spikes of Mn and O affirmed the existence of MnO_2 NSs. The Sm peak is ascribed to the doping of Sm, while the sodium (Na) spike resulted in NaOH to sustain the sample's pH. The potassium (K) high was observed as a precursor $KMnO_4$ used to synthesize MnO_2. Au peaks in spectra were attributed to the coating sprayed onto the samples to decrease the charging effects.

The topography and micro-structure of pristine and doped MnO_2 were confirmed by TEM (Fig. 4a-d). Long Burr-like morphology of undoped MnO_2 revealed as shown in Fig. 4a. Incorporation of Cs demonstrated that long burrs combined, which led to the formation of the aggregated cluster as explained in Fig. 4b. Addition of Sm showed that agglomerated cluster dispersed (Fig. 4c) and higher concentration of Sm determined the disruption of long burrs as illustrated in Fig. 4d.

HR-TEM photographs were adapted to determine inter-planner d-spacing, as indicated in Fig. S2. The d-spacing was calculated as 0.40 nm for MnO_2, allot the plane as (110). Furthermore, the interlayer d-spacing for Cs-doped MnO_2, and (2 and 4%) Sm/Cs-doped MnO_2 were 0.25, 0.17, and 0.13 nm, respectively.

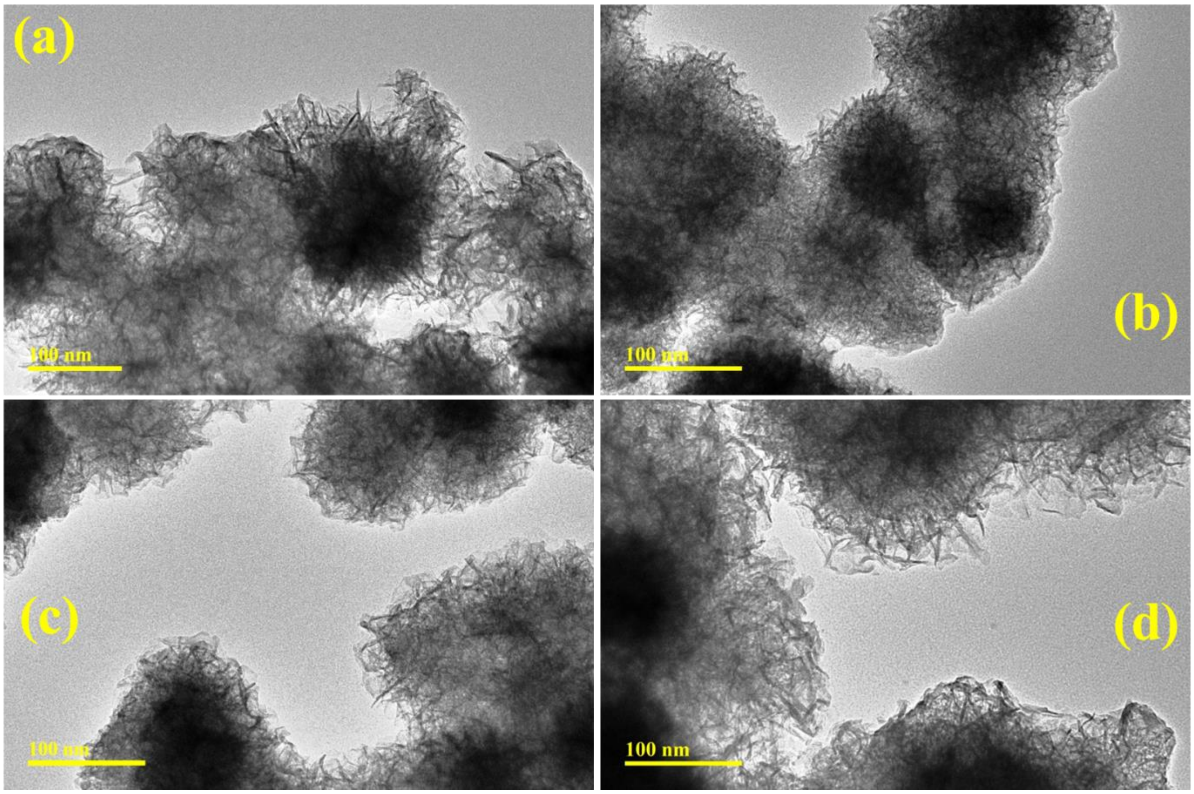

Fig. 4: TEM images of (a) MnO_2 (b) Cs-doped MnO_2, and (c-d) (2 and 4%) Sm/Cs-doped MnO_2.

The reducing agent ($NaBH_4$), oxidizing agent (RhB dye), and catalysts (Sm/Cs doped-MnO_2) were the main components of the catalytic process. Notably, the decolorization of RhB in the presence of $NaBH_4$ progressed slowly. In general, catalysts accelerate the reactions in ongoing research work, elaborated in Fig. S3. However, using the proper catalyst concentration is essential for the dye decolorization experiment. The reduction process initiates with transferring BH^{4-} ions from $NaBH_4$ to RhB molecules dissolved in an aqueous solution to the surface of Sm/Cs-doped MnO_2. The nanocatalysts (NCs) serve as an electron relay system, accelerating the transfer of electrons from the donor to the acceptor and RhB decolorized into leucorhodamine RhB (LRhB). NSs increase the adsorption of BH_4^- ions and dye molecules, whereas an increase in the number of interacting areas promotes rapid interaction between them, leading to efficient dye decomposition [60].

The catalytic activity of undoped and (2 and 4%) Sm/Cs-doped MnO_2 NSs with $NaBH_4$ for the reduction of RhB was investigated using a UV-vis spectrometer (Fig. 5). The pH of the solution and the prepared NCs in RhB dye released at a range of pH levels, influence the degradation rate. All synthesized samples exhibited maximum degradation of 71.42, 71.28, 74.42, and 78% in acidic (pH = 2.5) and 76.42, 75.71, 74.12, and 75.57% in basic (pH = 12), 79.33, 82.44, 87.22 and 91% in neutral (pH = 7) media. In contrast to the alkaline medium, both acidic and neutral environments showed the highest RhB reduction. The degradation seemed to be higher at pH=7; this might be owing to RhB exists in two primary forms in water, zwitter ionic ($RhB^{\pm}$) and cationic (RhB^{+}). As a consequence, in an acid or alkaline solution, both the dye and the catalyst exhibited electrostatic repulsion, and the catalytic efficacies of the Sm/Cs-doped MnO_2 were lower than in a neutral environment [61]. In an acidic environment, maximum degradation efficiency was ascribed to the H^{+} ions production [62]. After incorporating Cs, catalytic efficiency increased in all mediums attributed to the surface area was effectively increased for reaction [63]. In all media, the integration of 4% Sm had the highest degradation rate as it increased oxygen storage capacity [64].

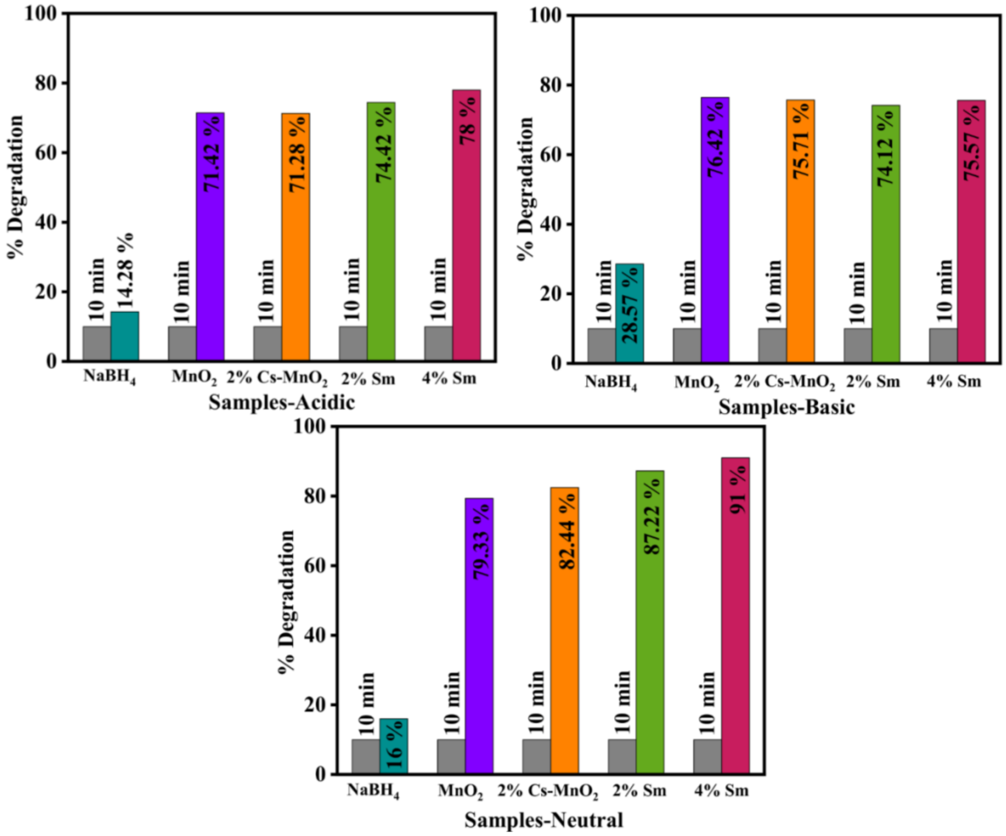

Fig. 5 Catalytic activity of MnO_2, Cs-doped MnO_2, and Sm (2 and 4 wt. %)/Cs-doped MnO_2 NSs in (a) acidic (b) alkaline, and (c) neutral media.

Table 1 Microbicidal efficacy of MnO_2 and Sm/Cs doped-MnO_2 NSs

Samples	Inhibition areas (mm)	
	500 µg/50 µL	1000 µg/50 µL
MnO_2	1.05	1.95
2% Cs- MnO_2	1.35	2.15

2% Sm	1.65	2.55
4% Sm	2.25	2.85
Positive standard	4.95	4.95
Negative standard	0	0

Well-diffusion method was employed to evaluate the bactericidal efficacy of pristine and Sm/CS doped-MnO_2, through the measurement of inhibition zones againt *E. coli*, as depicted in Table 1. *E. coli* inhibition zones were from 1.05–2.25 mm and 1.95–2.85 mm for low and high dosage concentrations, respectively. The inhibition zones were compared to ciprofloxacin (positive control), with an inhibition diameter of 4.95 mm, and DI water (negative control) with 0 mm zone. Pure MnO_2 was less effective against *E. coli* than Sm/Cs-doped MnO_2. The increase in bactericidal potential was observed after the integration of Cs ascribed to the enormous surface area of CS [63]. The antibacterial activity of MnO_2 NSs doped with Sm^{3+} was higher than undoped MnO_2, owing to the presence of oxygen vacancies [65].

Bactericidal action is associated with decreased cell membrane integrity, the formation of free radicals, and the generation of ROS (O^{2-}, HO_2, OH, and H_2O_2) [66,67]. Electron-donating properties of metal oxide produce ROS. Owing to the nanoscale-sized porous membrane of a microbial, nanomaterial with a strong charge and size can damage the membrane. These nanoparticles cause DNA and protein damage, disrupting cell function and eventually destroying cell performance (Fig. S4) [68].

Numerous studies have examined the bactericidal potential of nanoparticles containing metal ions [69–71]. The potential of nanoparticles for interaction with microorganisms through electrostatic, van der Waals, or hydrophobic properties is crucial to their microbicidal activity [72]. Enzymes from several metabolic processes required by microbial cells have been identified as significant candidates for antimicrobials development. Here we assess the inhibitory potential of Cs-doped MnO_2 and Cs/Sm-doped MnO_2 against *E. coli* DNA gyrase and FabB, enzymes from nucleic acid and fatty acid biosynthetic pathway.

Cs-doped MnO_2 has the most favorably docked shape in the functional domain of DNA Gyrase $B_{E.\ coli}$, exhibiting an H-bond interaction with K103, L115, and G117 with a docking score of 3.05. Conversely, Cs/Sm doped MnO_2 (binding score 5.39) formed an H-bond with K103, as seen in Fig. 6b.

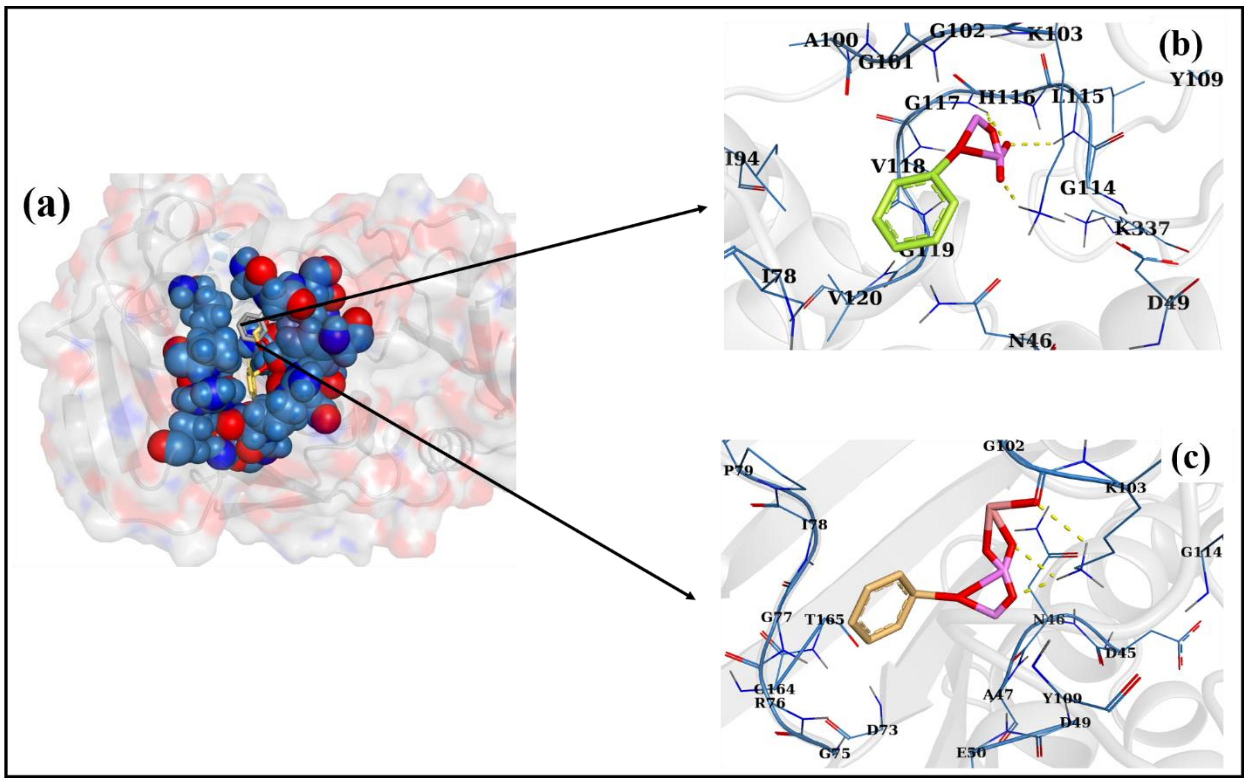

Fig. 6 (a). Nanocomposites-DNA gyrase$_{E.coli}$ docked complexes (superimposed), (b). Cs-doped MnO_2-DNA gyrase$_{E.coli}$ complex, (c). Cs/Sm doped MnO_2-DNA gyrase$_{E.coli}$ complex

The binding potential of these nanorods against $FabB_{E.\ coli}$ was also shown. It was demonstrated that Cs-doped MnO_2 forms H-bonded interactions with T300, T302, V304, and G305, with a cumulative binding score of 1.97. For Cs/Sm doped, MnO_2 docked within the active pocket of

FabB$_{E.\ Coli}$, the best binding score was 4.67, indicating a similar trend. As shown in Fig. 7b, amino acid residues such as T300 and T302 were implicated in H-bond interactions.

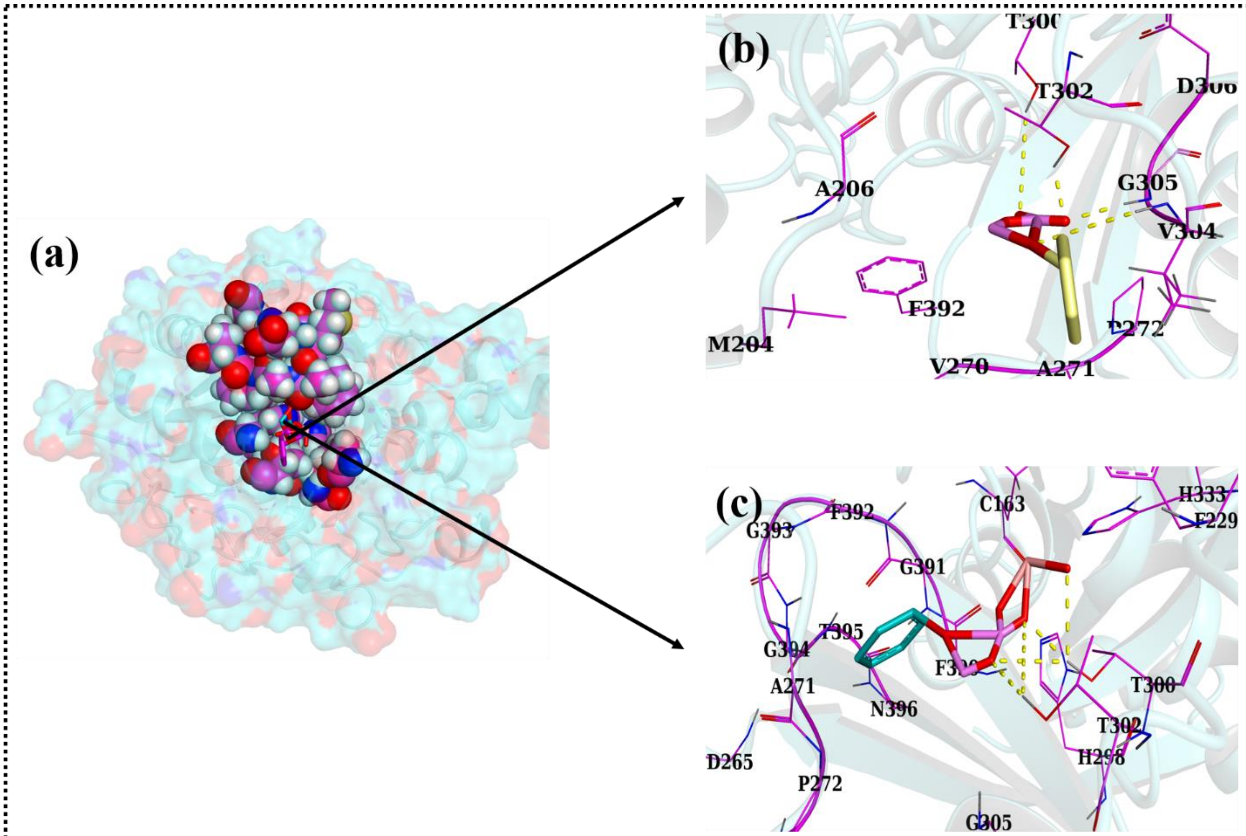

Fig. 7 (a). Nanocomposites FabB$_{E.coli}$ docked complexes (superimposed), (b). Cs-doped MnO_2-FabB$_{E.coli}$ complex, (c). Cs/Sm doped MnO_2-FabB $_{E.coli}$ complex

4. CONCLUSION

In this research, dopant-free and Sm/Cs doped-MnO_2 NSs were produced successfully to improve catalytic and bactericidal activity. Among all prepared samples, Sm/Cs doped-MnO_2 with 4% concentration exhibited effective antimicrobial and catalytic activity at 2.85 and 91%, respectively. FTIR revealed a significant band at 584 cm^{-1} for MnO_2 NSs. Burr-like morphology of MnO_2 NSs was observed, and the optical properties and band gap (2.13, 2.37, 2.27, and 2.17 eV) were calculated through a UV-vis spectrophotometer. In conclusion, Sm/Cs doped-MnO_2 NSs were expressed to be effective against infections and catalytic dye decomposition while also being inexpensive and ecologically benign. Cs/Sm doped MnO_2 was proposed as a potential blocker of FabB and DNA gyrase enzymes in vitro experiments.

Acknowledgment: Authors are thankful to HEC, Pakistan 20-17615 and authors express their appreciation to the Deanship of Scientific Research at King Khalid University, Saudi Arabia, for funding this work through research group program under grant number RGP. 2/428/44.

Conflict of Interest: The authors declare "no conflict of interest."

Data availability statement: On demand

REFERENCES

[1] R.H. Waghchaure, V.A. Adole, B.S. Jagdale, Photocatalytic degradation of methylene blue, rhodamine B, methyl orange and Eriochrome black T dyes by modified ZnO nanocatalysts: A concise review, Inorg. Chem. Commun. 143 (2022). https://doi.org/10.1016/j.inoche.2022.109764.

[2] M. Zhang, C. Zhang, X. Zhai, F. Luo, Y. Du, C. Yan, Antibacterial mechanism and activity of cerium oxide nanoparticles, Sci. China Mater. 62 (2019) 1727–1739. https://doi.org/10.1007/s40843-019-9471-7.

[3] V. Shah, S. Shah, H. Shah, F.J. Rispoli, K.T. McDonnell, S. Workeneh, A. Karakoti, A. Kumar, S. Seal, Antibacterial Activity of Polymer Coated Cerium Oxide Nanoparticles, PLoS One. 7 (2012). https://doi.org/10.1371/journal.pone.0047827.

[4] M. Aadil, A. Rahman, S. Zulfiqar, I.A. Alsafari, M. Shahid, I. Shakir, P.O. Agboola, S. Haider, M.F. Warsi, Facile synthesis of binary metal substituted copper oxide as a solar

light driven photocatalyst and antibacterial substitute, Adv. Powder Technol. 32 (2021) 940–950. https://doi.org/10.1016/j.apt.2021.01.040.

[5] M. Aadil, M. Mahmood, M.F. Warsi, I.A. Alsafari, S. Zulfiqar, M. Shahid, Fabrication of MnO2 nanowires and their nanohybrid with flat conductive matrix for the treatment of industrial effluents, FlatChem. 30 (2021) 100316. https://doi.org/10.1016/j.flatc.2021.100316.

[6] M.S. Lucas, J.A. Peres, Decolorization of the azo dye Reactive Black 5 by Fenton and photo-Fenton oxidation, Dye. Pigment. 71 (2006) 236–244. https://doi.org/10.1016/j.dyepig.2005.07.007.

[7] Y. Dong, K. He, B. Zhao, Y. Yin, L. Yin, A. Zhang, Catalytic ozonation of azo dye active brilliant red X-3B in water with natural mineral brucite, Catal. Commun. 8 (2007) 1599–1603. https://doi.org/10.1016/j.catcom.2007.01.016.

[8] Y. Liu, X. Chen, J. Li, C. Burda, Photocatalytic degradation of azo dyes by nitrogen-doped TiO2 nanocatalysts, Chemosphere. 61 (2005) 11–18. https://doi.org/10.1016/j.chemosphere.2005.03.069.

[9] A. Aguedach, S. Brosillon, J. Morvan, E.K. Lhadi, Photocatalytic degradation of azo-dyes reactive black 5 and reactive yellow 145 in water over a newly deposited titanium dioxide, Appl. Catal. B Environ. 57 (2005) 55–62. https://doi.org/10.1016/j.apcatb.2004.10.009.

[10] A. Rahman, M. Aadil, S. Zulfiqar, I.A. Alsafari, M. Shahid, P.O. Agboola, M.F. Warsi, M.E.F. Abdel-Haliem, Fabrication of binary metal substituted CdO with superior aptitude for dye degradation and antibacterial activity, Ceram. Int. 47 (2021) 8082–8093. https://doi.org/10.1016/j.ceramint.2020.11.163.

[11] J. Hassan, M. Ikram, A. Ul-Hamid, M. Imran, M. Aqeel, S. Ali, Application of Chemically Exfoliated Boron Nitride Nanosheets Doped with Co to Remove Organic Pollutants Rapidly from Textile Water, Nanoscale Res. Lett. 15 (2020). https://doi.org/10.1186/s11671-020-03315-y.

[12] M. Ikram, J. Hassan, A. Raza, A. Haider, S. Naz, A. Ul-Hamid, J. Haider, I. Shahzadi, U. Qamar, S. Ali, Photocatalytic and bactericidal properties and molecular docking analysis of TiO2nanoparticles conjugated with Zr for environmental remediation, RSC Adv. 10 (2020) 30007–30024. https://doi.org/10.1039/d0ra05862a.

[13] Z. Yin, B. Chen, M. Bosman, X. Cao, J. Chen, B. Zheng, H. Zhang, Au nanoparticle-modified MoS2 nanosheet-based photoelectrochemical cells for water splitting, Small. 10 (2014) 3537–3543. https://doi.org/10.1002/smll.201400124.

[14] M.H. Cho, J. Ju, S.J. Kim, H. Jang, Tribological properties of solid lubricants (graphite, Sb2S3, MoS2) for automotive brake friction materials, Wear. 260 (2006) 855–860. https://doi.org/10.1016/j.wear.2005.04.003.

[15] H. Salomon, C. Vignaud, S. Lahlil, N. Menguy, Solutrean and Magdalenian ferruginous rocks heat-treatment: Accidental and/or deliberate action?, J. Archaeol. Sci. 55 (2015) 100–112. https://doi.org/10.1016/j.jas.2014.12.024.

[16] S.Y. Chen, W. Song, H.J. Lin, S. Wang, S. Biswas, M. Mollahosseini, C.H. Kuo, P.X. Gao, S.L. Suib, Manganese Oxide Nanoarray-Based Monolithic Catalysts: Tunable Morphology and High Efficiency for CO Oxidation, ACS Appl. Mater. Interfaces. 8 (2016) 7834–7842. https://doi.org/10.1021/acsami.6b00578.

[17] M.F. Warsi, K. Chaudhary, S. Zulfiqar, A. Rahman, I.A. Al Safari, H.M. Zeeshan, P.O.

Agboola, M. Shahid, M. Suleman, Copper and silver substituted MnO2 nanostructures with superior photocatalytic and antimicrobial activity, Ceram. Int. 48 (2022) 4930–4939. https://doi.org/10.1016/j.ceramint.2021.11.031.

[18] T.D. Dang, A.N. Banerjee, Q.T. Tran, S. Roy, Fast degradation of dyes in water using manganese-oxide-coated diatomite for environmental remediation, J. Phys. Chem. Solids. 98 (2016) 50–58. https://doi.org/10.1016/j.jpcs.2016.06.006.

[19] N.A. Fathy, S.E. El-Shafey, O.I. El-Shafey, W.S. Mohamed, Oxidative degradation of RB19 dye by a novel γ-MnO2/MWCNT nanocomposite catalyst with H2O2, J. Environ. Chem. Eng. 1 (2013) 858–864. https://doi.org/10.1016/j.jece.2013.07.028.

[20] P. Franco, O. Sacco, I. De Marco, D. Sannino, V. Vaiano, Photocatalytic Degradation of Eriochrome Black-T Azo Dye Using Eu-Doped ZnO Prepared by Supercritical Antisolvent Precipitation Route: A Preliminary Investigation, Top. Catal. 63 (2020) 1193–1205. https://doi.org/10.1007/s11244-020-01279-y.

[21] R. Li, J. Yang, S. Xu, Y. Zhou, X. Wang, H. Peng, J. Du, Preparation of Gd-doped TiO2 nanotube arrays by anodization method and its photocatalytic activity for methyl orange degradation, Catalysts. 10 (2020). https://doi.org/10.3390/catal10030298.

[22] K.A. Malik, J.H. Malik, A.A. Bhat, I. Assadullah, R. Tomar, Trap assisted visible light luminescent properties of hydrothermally grown Gd doped ZnO nanostructures, Vacuum. 183 (2021). https://doi.org/10.1016/j.vacuum.2020.109832.

[23] S. Selvaraj, S. Patrick D, G.A. Vangari, M.K. Mohan, P. S, M. C, Facile synthesis of Sm doped ZnO nanoflowers by Co-precipitation method for enhanced photocatalytic degradation of MB dye under sunlight irradiation, Ceram. Int. 48 (2022) 29049–29058.

https://doi.org/10.1016/j.ceramint.2022.04.299.

[24] M.T. Ramesan, T. Sampreeth, In situ synthesis of polyaniline/Sm-doped TiO2 nanocomposites: evaluation of structural, morphological, conductivity studies and gas sensing applications, J. Mater. Sci. Mater. Electron. 29 (2018) 4301–4311. https://doi.org/10.1007/s10854-017-8377-1.

[25] J. Dou, S. Yin, J.Y. Chong, B. Zhang, J. Han, Y. Huang, R. Xu, Carbon spheres anchored Co3O4 nanoclusters as an efficient catalyst for dye degradation, Appl. Catal. A Gen. 513 (2016) 106–115. https://doi.org/10.1016/j.apcata.2015.12.028.

[26] M. Aamir, I. Bibi, S. Ata, F. Majid, S. Kamal, N. Alwadai, M. Sultan, S. Iqbal, M. Aadil, M. Iqbal, Graphene oxide nanocomposite with Co and Fe doped LaCrO3 perovskite active under solar light irradiation for the enhanced degradation of crystal violet dye, J. Mol. Liq. 322 (2021). https://doi.org/10.1016/j.molliq.2020.114895.

[27] Bergey's Manual of Systematics of Archaea and Bacteria, Wiley, 2015. https://doi.org/10.1002/9781118960608.

[28] A.W. Bauer, W.M. Kirby, J.C. Sherris, M. Turck, Antibiotic susceptibility testing by a standardized single disk method., Am. J. Clin. Pathol. 45 (1966) 493–496. https://doi.org/10.1093/ajcp/45.4_ts.493.

[29] F. Adzitey, S. Yussif, R. Ayamga, S. Zuberu, F. Addy, G. Adu-Bonsu, N. Huda, R. Kobun, Antimicrobial Susceptibility and Molecular Characterization of Escherichia coli Recovered from Milk and Related Samples, Microorganisms. 10 (2022). https://doi.org/10.3390/microorganisms10071335.

[30] Wayne PA, Performance standards for antimicrobial susceptibility testing., Clin. Lab. Stand. Inst. 24th Inter (2014) 1–182. https://cir.nii.ac.jp/crid/1130855721503969931 (accessed April 8, 2023).

[31] B.A. Iwalokun, A. Ogunledun, D.O. Ogbolu, S.B. Bamiro, J. Jimi-Omojola, In vitro antimicrobial properties of aqueous garlic extract against multidrug-resistant bacteria and Candida species from Nigeria, J. Med. Food. 7 (2004) 327–333. https://doi.org/10.1089/jmf.2004.7.327.

[32] A. Haider, M. Ijaz, M. Imran, M. Naz, H. Majeed, J.A. Khan, M.M. Ali, M. Ikram, Enhanced bactericidal action and dye degradation of spicy roots' extract-incorporated fine-tuned metal oxide nanoparticles, Appl. Nanosci. 10 (2020) 1095–1104. https://doi.org/10.1007/s13204-019-01188-x.

[33] A. Haider, M. Ijaz, S. Ali, J. Haider, M. Imran, H. Majeed, I. Shahzadi, M.M. Ali, J.A. Khan, M. Ikram, Green Synthesized Phytochemically (Zingiber officinale and Allium sativum) Reduced Nickel Oxide Nanoparticles Confirmed Bactericidal and Catalytic Potential, Nanoscale Res. Lett. 15 (2020). https://doi.org/10.1186/s11671-020-3283-5.

[34] H.Q. Li, L. Shi, Q.S. Li, P.G. Liu, Y. Luo, J. Zhao, H.L. Zhu, Synthesis of C(7) modified chrysin derivatives designing to inhibit β-ketoacyl-acyl carrier protein synthase III (FabH) as antibiotics, Bioorganic Med. Chem. 17 (2009) 6264–6269. https://doi.org/10.1016/j.bmc.2009.07.046.

[35] Z. Mehmood, M. Ikram, M. Imran, A. Shahzadi, A. Haider, A. Ul-Hamid, W. Nabgan, J. Haider, S. Hayat, Z. officinale-doped silver/calcium oxide nanocomposites: Catalytic activity and antimicrobial potential with molecular docking analysis, Process Biochem.

121 (2022) 635–646. https://doi.org/10.1016/j.procbio.2022.07.035.

[36] N.L.S. Lee, K.Y. Yuen, C.R. Kumana, β-Lactam antibiotic and β-lactamase inhibitor combinations, JAMA. 285 (2001) 386–388. https://doi.org/10.1001/jama.285.4.386.

[37] F. V. Stanger, C. Dehio, T. Schirmer, Structure of the N-Terminal Gyrase B fragment in complex with ADP?Pi reveals rigid-body motion induced by ATP hydrolysis, PLoS One. 9 (2014). https://doi.org/10.1371/journal.pone.0107289.

[38] A.C. Price, K.H. Choi, R.J. Heath, Z. Li, S.W. White, C.O. Rock, Inhibition of β-ketoacyl-acyl carrier protein synthases by thiolactomycin and cerulenin: Structure and mechanism, J. Biol. Chem. 276 (2001) 6551–6559. https://doi.org/10.1074/jbc.M007101200.

[39] A. Ul-Hamid, H. Dafalla, A.S. Hakeem, A. Haider, M. Ikram, In-Vitro Catalytic and Antibacterial Potential of Green Synthesized CuO Nanoparticles against Prevalent Multiple Drug Resistant Bovine Mastitogen Staphylococcus aureus, Int. J. Mol. Sci. 23 (2022). https://doi.org/10.3390/ijms23042335.

[40] I. Shahzadi, M. Islam, H. Saeed, A. Haider, A. Shahzadi, J. Haider, N. Ahmed, A. Ul-Hamid, W. Nabgan, M. Ikram, H.A. Rathore, Formation of biocompatible MgO/cellulose grafted hydrogel for efficient bactericidal and controlled release of doxorubicin, Int. J. Biol. Macromol. 220 (2022) 1277–1286. https://doi.org/10.1016/j.ijbiomac.2022.08.142.

[41] M. Ikram, K. Chaudhary, A. Shahzadi, A. Haider, I. Shahzadi, A. Ul-Hamid, N. Abid, J. Haider, W. Nabgan, A.R. Butt, Chitosan/starch-doped MnO2 nanocomposite served as dye degradation, bacterial activity, and insilico molecular docking study, Mater. Today Nano. 20 (2022). https://doi.org/10.1016/j.mtnano.2022.100271.

[42] A. Faisal, A. Abadi, A.D. Faisal, A.A. Aljubouri, Synthesis and Production of Carbon Nanospheres Using Noncatalytic CVD Method, Int. J. Adv. Mater. Res. 2 (2016) 86–91. https://www.researchgate.net/profile/Ali-Abadi/publication/313105476_Synthesis_and_Production_of_Carbon_Nanospheres_Using_Noncatalytic_CVD_Method/links/58904ce192851c9794c66973/Synthesis-and-Production-of-Carbon-Nanospheres-Using-Noncatalytic-CVD-Method.p (accessed April 8, 2023).

[43] M. Faraz, F.K. Naqvi, M. Shakir, N. Khare, Synthesis of samarium-doped zinc oxide nanoparticles with improved photocatalytic performance and recyclability under visible light irradiation, New J. Chem. 42 (2018) 2295–2305. https://doi.org/10.1039/c7nj03927a.

[44] M. Wang, J. Han, P. Guo, M. Sun, Y. Zhang, Z. Tong, M. You, C. Lv, Hydrothermal synthesis of B-doped Bi2MoO6 and its high photocatalytic performance for the degradation of Rhodamine B, J. Phys. Chem. Solids. 113 (2018) 86–93. https://doi.org/10.1016/j.jpcs.2017.10.019.

[45] M. Aadil, A.G. Taki, S. Zulfiqar, A. Rahman, M. Shahid, M.F. Warsi, Z. Ahmad, A.A. Alothman, S. Mohammad, Gadolinium doped zinc ferrite nanoarchitecture reinforced with a carbonaceous matrix: a novel hybrid material for next-generation flexible capacitors, RSC Adv. 13 (2023) 28063–28075. https://doi.org/10.1039/d3ra05290g.

[46] M. Rashid, W. Hassan, M. Aadil, H.H. Somaily, N.M. Mahdi, R. Lataef, A.G. Taki, K. Srithilat, D.F. Baamer, S.M. Albukhari, M.A. Salam, A. Llyas, Solar-light-driven and magnetically recoverable doped nano-ferrite: An ideal photocatalyst for water purification applications, Opt. Mater. (Amst). 135 (2023).

https://doi.org/10.1016/j.optmat.2022.113192.

[47] S. Majumdar, The effects of crystallite size, surface area and morphology on the sensing properties of nanocrystalline SnO2 based system, Ceram. Int. 41 (2015) 14350–14358. https://doi.org/10.1016/j.ceramint.2015.07.068.

[48] Y.S. Danilov, Effect of grain size on the Bauschinger effect, Met. Sci. Heat Treat. 6 (1964) 563–565. https://doi.org/10.1007/BF00652409.

[49] M. Aadil, W. Hassan, H.H. Somaily, S.R. Ejaz, R.R. Abass, H. Jasem, S.K. Hachim, A.H. Adhab, E.S. Abood, I.A. Alsafari, Synergistic effect of doping and nanotechnology to fabricate highly efficient photocatalyst for environmental remediation, J. Alloys Compd. 920 (2022). https://doi.org/10.1016/j.jallcom.2022.165876.

[50] E. Bartonickova, J. Cihlar, K. Castkova, Microwave-assisted synthesis of bismuth oxide, Process. Appl. Ceram. 1 (2007) 29–33. https://doi.org/10.2298/pac0702029b.

[51] W. Raza, M.M. Haque, M. Muneer, T. Harada, M. Matsumura, Synthesis, characterization and photocatalytic performance of visible light induced bismuth oxide nanoparticle, J. Alloys Compd. 648 (2015) 641–650. https://doi.org/10.1016/j.jallcom.2015.06.245.

[52] K. Rout, M. Mohapatra, S. Anand, A critical analysis of cation adsorption from single and binary solutions on low surface area β-MnO 2, Appl. Surf. Sci. 270 (2013) 205–218. https://doi.org/10.1016/j.apsusc.2013.01.002.

[53] S. Dhingra, T. Chhabra, V. Krishnan, C.M. Nagaraja, Visible-Light-Driven Selective Oxidation of Biomass-Derived HMF to DFF Coupled with H2Generation by Noble Metal-Free Zn0.5Cd0.5S/MnO2Heterostructures, ACS Appl. Energy Mater. 3 (2020) 7138–

7148. https://doi.org/10.1021/acsaem.0c01189.

[54] K. Skrabania, A. Miasnikova, A.M. Bivigou-Koumba, D. Zehm, A. Laschewsky, Examining the UV-vis absorption of RAFT chain transfer agents and their use for polymer analysis, Polym. Chem. 2 (2011) 2074–2083. https://doi.org/10.1039/c1py00173f.

[55] B.A. Pinaud, Z. Chen, D.N. Abram, T.F. Jaramillo, Thin films of sodium birnessite-type MnO2: Optical properties, electronic band structure, and solar photoelectrochemistry, J. Phys. Chem. C. 115 (2011) 11830–11838. https://doi.org/10.1021/jp200015p.

[56] R. Zamiri, A.F. Lemos, A. Reblo, H.A. Ahangar, J.M.F. Ferreira, Effects of rare-earth (Er, la and Yb) doping on morphology and structure properties of ZnO nanostructures prepared by wet chemical method, Ceram. Int. 40 (2014) 523–529. https://doi.org/10.1016/j.ceramint.2013.06.034.

[57] H.Y. He, J. Fei, J. Lu, Sm-doping effect on optical and electrical properties of ZnO films, J. Nanostructure Chem. 5 (2015) 169–175. https://doi.org/10.1007/s40097-015-0147-0.

[58] P. Velusamy, R.R. Babu, K.T. Aparna, Effect of Sm doping on the physical properties of ZnO thin films deposited by spray pyrolysis technique, in: AIP Conf. Proc., American Institute of Physics Inc., 2017. https://doi.org/10.1063/1.4980545.

[59] M.M. Ba-Abbad, M.S. Takriff, A. Benamor, M.S. Nasser, E. Mahmoudi, A.W. Mohammad, Synthesis and characterization of Sm3+-doped ZnO nanoparticles via a sol–gel method and their photocatalytic application, J. Sol-Gel Sci. Technol. 85 (2018) 178–190. https://doi.org/10.1007/s10971-017-4503-z.

[60] A. Bari, M. Ikram, A. Haider, A. Ul-Hamid, J. Haider, I. Shahzadi, G. Nazir, A. Shahzadi,

M. Imran, A. Ghaffar, Evaluation of bactericidal potential and catalytic dye degradation of multiple morphology based chitosan/polyvinylpyrrolidone-doped bismuth oxide nanostructures, Nanoscale Adv. 4 (2022) 2713–2728. https://doi.org/10.1039/d2na00105e.

[61] Y. Chen, B. Zhai, Y. Liang, Enhanced degradation performance of organic dyes removal by semiconductor/MOF/graphene oxide composites under visible light irradiation, Diam. Relat. Mater. 98 (2019). https://doi.org/10.1016/j.diamond.2019.107508.

[62] A. Rafique, M. Ikram, A. Haider, A. Ul-Hamid, S. Naz, W. Nabgan, J. Haider, I. Shahzadi, Dye degradation, antibacterial activity and molecular docking analysis of cellulose/polyvinylpyrrolidone-doped cadmium sulphide quantum dots, Int. J. Biol. Macromol. 214 (2022) 264–277. https://doi.org/10.1016/j.ijbiomac.2022.06.058.

[63] A.A. Deshmukh, S.D. Mhlanga, N.J. Coville, Carbon spheres, Mater. Sci. Eng. R Reports. 70 (2010) 1–28. https://doi.org/10.1016/j.mser.2010.06.017.

[64] T. Deng, C. Zhang, Y. Xiao, A. Xie, Y. Pang, Y. Yang, One-step synthesis of samarium-doped ceria and its CO catalysis, Bull. Mater. Sci. 38 (2015) 1149–1154. https://doi.org/10.1007/s12034-015-0994-9.

[65] A. Balamurugan, M. Sudha, S. Surendhiran, R. Anandarasu, S. Ravikumar, Y.A. Syed Khadar, Hydrothermal synthesis of samarium (Sm) doped cerium oxide (CeO2) nanoparticles: Characterization and antibacterial activity, in: Mater. Today Proc., 2019: pp. 3588–3594. https://doi.org/10.1016/j.matpr.2019.08.217.

[66] S. Meghana, P. Kabra, S. Chakraborty, N. Padmavathy, Understanding the pathway of antibacterial activity of copper oxide nanoparticles, RSC Adv. 5 (2015) 12293–12299. https://doi.org/10.1039/c4ra12163e.

[67] S. Jadhav, S. Gaikwad, M. Nimse, A. Rajbhoj, Copper Oxide Nanoparticles: Synthesis, Characterization and Their Antibacterial Activity, J. Clust. Sci. 22 (2011) 121–129. https://doi.org/10.1007/s10876-011-0349-7.

[68] C.Z. Chen, S.L. Cooper, Interactions between dendrimer biocides and bacterial membranes, Biomaterials. 23 (2002) 3359–3368. https://doi.org/10.1016/S0142-9612(02)00036-4.

[69] T. Shujah, A. Shahzadi, A. Haider, M. Mustajab, A.M. Haider, A. Ul-Hamid, J. Haider, W. Nabgan, M. Ikram, Molybdenum-doped iron oxide nanostructures synthesized via a chemical co-precipitation route for efficient dye degradation and antimicrobial performance: in silico molecular docking studies, RSC Adv. 12 (2022) 35177–35191. https://doi.org/10.1039/d2ra07238f.

[70] M. Ikram, A. Haider, M. Imran, J. Haider, A. Ul-Hamid, A. Shahzadi, R. Malik, Kashaf-Ul-Ain, W. Nabgan, G. Nazir, S. Ali, Graphitic-C3N4/chitosan-doped NiO nanostructure to treat the polluted water and their bactericidal with in silico molecular docking analysis, Int. J. Biol. Macromol. 227 (2023) 962–973. https://doi.org/10.1016/j.ijbiomac.2022.11.273.

[71] M. Ikram, H. Maghfoor, A. Shahzadi, A. Haider, I. Shahzadi, N. Abid, A. Ul-Hamid, J. Haider, W. Nabgan, A.R. Butt, Towards effective dye degradation and antimicrobial behavior of chitosan and C3N4-doped CdS nanoparticles, Mater. Today Commun. 33 (2022). https://doi.org/10.1016/j.mtcomm.2022.104814.

[72] S. Shaheen, A. Iqbal, M. Ikram, M. Imran, S. Naz, A. Ul-Hamid, A. Shahzadi, W. Nabgan, J. Haider, A. Haider, Graphene oxide-ZnO nanorods for efficient dye

degradation, antibacterial and in-silico analysis, Appl. Nanosci. 12 (2022) 165–177. https://doi.org/10.1007/s13204-021-02251-2.